
RAPTOR: RIDGE-ADAPTIVE LOGISTIC PROBES

Ziqi Gao, Yaotian Zhu, Qingcheng Zeng, Xu Zhao, Ziqing Wang, Feng Ruan, Kaize Ding

Northwestern University

kaize.ding@northwestern.edu

ABSTRACT

Probing studies what information is encoded in a frozen LLM’s **layer representations** by training a lightweight predictor on top of it. Beyond analysis, probes are often used operationally in *probe-then-steer* pipelines: a learned **concept vector** is extracted from a probe and then injected via additive activation steering by adding it to a layer representation during the forward pass. The effectiveness of this pipeline hinges on estimating concept vectors that are accurate, directionally stable under ablation, and inexpensive to obtain. Motivated by these desiderata, We propose RAPTOR (**R**idge-**A**daptive **L**ogistic **P**robe), a simple ℓ_2 -regularized logistic probe whose validation-tuned ridge strength yields concept vectors from normalized weights. Across extensive experiments on instruction-tuned LLMs and human-written concept datasets, RAPTOR matches or exceeds strong baselines in accuracy while achieving competitive directional stability and substantially lower training cost; these quantitative results are supported by qualitative downstream steering demonstrations. Finally, using the Convex Gaussian Min–max Theorem (CGMT), we provide a mechanistic characterization of ridge logistic regression in an idealized Gaussian teacher–student model in the high-dimensional few-shot regime, explaining how penalty strength λ mediates probe accuracy and concept-vector stability, yielding structural predictions that qualitatively align with trends observed on real LLM embeddings.

Keywords large language models · activation steering · representation steering · concept vectors · probing, interpretability · robustness · logistic probes · ridge regularization

1 Introduction

Probing elucidates the information encoded within a frozen model’s internal layers by training a lightweight auxiliary predictor [Alain and Bengio, 2016, Belinkov et al., 2017, Hewitt and Manning, 2019, Tenney et al., 2019]. The standard procedure involves collecting input texts with binary labels for a target concept, performing a forward pass to extract activations, and training a classifier on these representations. This technique offers dual utility. First, it serves as a diagnostic tool to quantify how strongly a concept is captured within the model’s internal state. Second, it functions operationally, as the trained probe identifies a direction in the representation space suitable for downstream interventions.

A primary application in this work is *steering*, defined as the modulation of behavior at inference time without updating model weights [Dathathri et al., 2019, Krause et al., 2021, Liu et al., 2021]. Within this domain, we focus on *additive activation steering*, a technique that modifies a layer’s representation by injecting a learned direction [Turner et al., 2023a, Rimsky et al., 2024]. For an input sentence x tokenized as (t_1, \dots, t_T) , let $h_{\ell,T} \in \mathbb{R}^p$ denote the **layer representation** of the last token at layer $\ell \in \{1, \dots, L\}$. Consistent with standard probing practices, we treat $h_{\ell,T}$ as a sentence-level summary. Additive activation steering intervenes by directly editing this representation:

$$h_{\ell,T} \leftarrow h_{\ell,T} + \alpha v_{\ell}, \quad (1)$$

where $v_{\ell} \in \mathbb{R}^p$ represents the **concept vector** for the target concept at layer ℓ , and $\alpha \in \mathbb{R}$ controls the steering strength. This approach is particularly advantageous as it is simple to implement and imposes negligible inference overhead. However, its effectiveness is contingent upon the quality of v_{ℓ} (and α); if the estimated concept vector is noisy or brittle, the resulting steering becomes unreliable.

What is a good probe? Given that probes are frequently trained with limited supervision, an effective probe must satisfy three requirements that directly determine downstream usability: **(i) accuracy**: it must reliably predict the concept label from the layer representation; **(ii) directional stability**: the learned direction must remain consistent under minor training perturbations (e.g., resampling, dataset variations, or mild distribution shifts), ensuring the concept vector is reusable rather than dataset-specific [Hewitt and Liang, 2019, Pimentel et al., 2020]; and **(iii) computational efficiency**: training and tuning must be inexpensive, as probing is typically conducted across numerous layers, concepts, and models. While existing literature predominantly emphasizes (i), criteria (ii) and (iii) are critical when probes function as components within broader pipelines, such as probe–then–steer workflows. These criteria will serve as a useful lens for comparing probe choices throughout the paper.

Motivated by these desiderata, we propose **RAPTOR: Ridge-Adaptive Logistic Probes**. For each tuple (model, layer, concept), RAPTOR fits a single ℓ_2 -regularized logistic regression probe on frozen layer representations and uses its normalized weight vector as the concept vector v_ℓ . The method relies on one essential hyperparameter: the ridge regularization strength λ , which is selected via validation. Despite its simplicity, this design directly targets the practical requirements outlined above: logistic regression provides a strong linear baseline for accuracy, while ridge regularization improves directional robustness in limited-data regimes. This minimalist design is necessary because existing alternatives often fail to balance these competing objectives. While many probe estimators exist [Belinkov, 2022], two persistent issues undermine their utility in probe-then-steer applications: (i) higher probe accuracy does not necessarily yield a reliable concept vector across small context changes [Ravichander et al., 2021, Agarwal et al., 2025, Tan et al., 2024]; and (ii) elaborate estimators frequently increase computational costs, thereby limiting the feasibility of extensive layer and model sweeps [Belinkov, 2022]. Consequently, we evaluate RAPTOR against these baselines using the tripartite metric of accuracy, stability, and cost.

We evaluate our approach through a comprehensive benchmark spanning instruction-tuned models, varied concept datasets, and the full depth of the network layers. Comparing RAPTOR against key alternatives, we find that it matches or exceeds the accuracy of strong baselines while providing greater directional stability and reduced training overhead. To validate these findings, we include qualitative steering examples showing that robust concept vectors translate directly into more reliable downstream control.

From a theoretical perspective, LLM probing often operates in a regime where the representation dimension p is large and can be comparable to the number of labeled samples n (sometimes n even smaller than p). In this setting, classical fixed- p asymptotics can be inaccurate, and ℓ_2 regularization is not merely a numerical stabilizer but a primary driver of concept vector’s quality. To clarify how the ridge strength λ shapes both probing accuracy and the stability of the estimated concept vector, we provide a self-contained high-dimensional analysis of ridge logistic regression under a Gaussian teacher–student model in the proportional limit $n, p \rightarrow \infty$ with $n/p \rightarrow \delta$. The resulting deterministic characterization yields an explicit prediction for out-of-sample performance in this idealized setting and explains λ as a stability knob for probes. Moreover, we demonstrate that these predictions capture the dominant performance trends on real datasets. Our main contributions are as follows:

- **Operator-aligned formulation** We formalize concept-vector estimation for additive activation steering and propose to benchmark probes under a joint objective capturing *accuracy*, *directional stability*, and *computational cost*.
- **RAPTOR algorithm** We introduce a one-knob ridge-logistic probing pipeline with explicit hyperparameter selection of λ , producing interpretable concept vectors suitable for additive activation steering.
- **Systematic evaluation** We conduct a multi-model, multi-dataset, multi-layer benchmark comparing RAPTOR against representative alternatives, clarifying when a tuned ridge-logistic probe matches or exceeds more elaborate estimators under the accuracy–stability–cost criteria.
- **Theory-backed interpretation** We provide a self-contained high-dimensional characterization of ridge logistic regression that explains how λ mediates accuracy and concept-vector stability in the proportional regime.

2 Related Work

Probing Probing studies what information is present in a model’s *layer representation* by training an auxiliary predictor on top of frozen activations. Early work popularized probes as diagnostic classifiers for neural representations [Alain and Bengio, 2016, Belinkov et al., 2017], and later work scaled this idea across layers and architectures to map where linguistic and semantic properties are encoded [Tenney et al., 2019, Hewitt and Manning, 2019]. Most commonly, a *linear probe* reads out a concept label with a linear classifier, while a *nonlinear probe* increases predictor expressivity (e.g., an MLP) to potentially improve accuracy; both are trained on the same layer representations. A substantial methodological literature emphasizes that probe conclusions can depend on modeling choices and evaluation protocols, and that predictive accuracy can conflate properties of the representation with properties of the probe [Hewitt and Liang, 2019, Pimentel et al., 2020, Voita and Titov, 2020, Ravichander et al., 2021, Belinkov, 2022]. Related lines of work

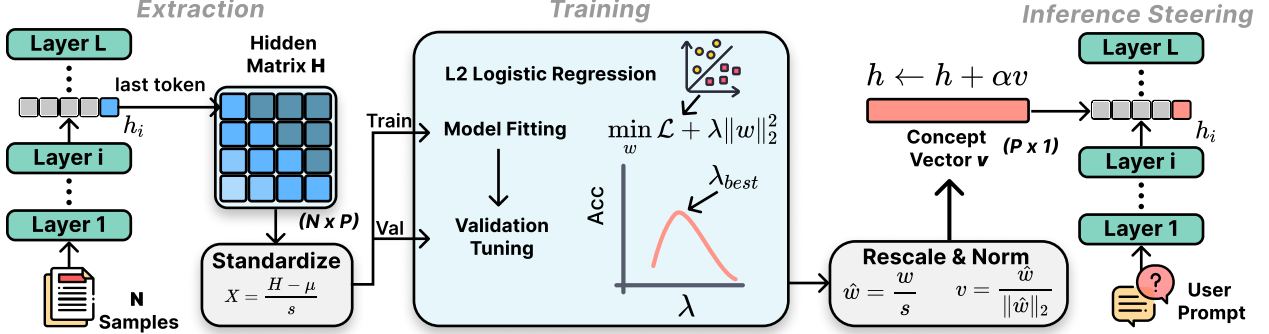


Figure 1: **Overview of the RAPTOR pipeline for additive activation steering:** extract layerwise last-token embeddings, standardize features, fit an ℓ_2 -regularized logistic probe with λ selected on a validation split, rescale to embedding space and normalize to obtain the concept vector v_ℓ , then steer at inference by $h_{\ell,T} \leftarrow h_{\ell,T} + \alpha v_\ell$.

interpret probe weights as directions (e.g., TCAV) [Kim et al., 2018], or use learned directions for editing/removal, such as iterative nullspace-based procedures [Ravfogel et al., 2020a,b] and amnesia removal [Elazar et al., 2021]. More recently, concept estimation has been extended beyond a single direction to *subspaces* or *distributions* over directions, including Gaussian Concept Subspace (GCS) [Zhao et al., 2024] and random-feature-model-based estimators (RFM) for scalable concept estimation [Beaglehole et al., 2025, Zhao et al., 2024].

Probe–then–steer pipelines A common way to obtain a *concept vector* for additive activation steering is to train a probe on frozen layer representations and reuse its learned direction as the intervention direction. This idea is explicit in TCAV-style concept vectors [Kim et al., 2018], and it underlies many recent activation-steering approaches that add a learned direction to internal activations [Turner et al., 2023b, Panickssery et al., 2023, Rimsky et al., 2024, Stolfo et al., 2024]. Within this pipeline, the intervention form is fixed (add a direction), so the main question becomes how to estimate a concept vector that is accurate, stable to small data/context perturbations, and inexpensive to obtain.

3 Methodology

3.1 Ridge-Adaptive Logistic Probe

The reason we use the ridge logistic regression is the high-dimensional, small-sample regime typical of probing: labeled hidden states are often (nearly) linearly separable (see Table 4). In this setting, the *unregularized* logistic objective need not admit a finite maximizer: when the data are separable, the likelihood can be increased without bound by sending $\|w\|_2 \rightarrow \infty$ along a separating direction. As a result, standard optimization procedures tend to keep growing the weight norm and may hit iteration limits or exhibit numerical issues (e.g., poor conditioning or overflow), which makes the baseline appear ‘unstable’ in practice. Introducing an ℓ_2 penalty restores existence and uniqueness, but a fixed, untuned regularization strength can still lead to poorly conditioned optimization and slow convergence, particularly when training probes at scale over many (model, layer, concept) configurations.

Accordingly, we adopt ℓ_2 -regularized logistic regression with validation-based selection of the ridge strength λ . This choice exposes a single, interpretable knob that governs both statistical regularization and training stability, while keeping the estimator minimal and allowing us to derive a high-dimensional characterization (section 5) that helps explain how λ shapes the observed accuracy–stability behavior.

Finally, our implementation attains practical efficiency via standard training configurations (e.g., warm starts and early stopping during training), detailed in section 3.1. We refer to the resulting procedure pipeline as RAPTOR.

Method Setup Fix a concept c and a model M . For each layer ℓ , we form a labeled dataset $\{(h_i^{(\ell)}, y_i)\}_{i=1}^N$ with $h_i^{(\ell)} \in \mathbb{R}^p$ and $y_i \in \{0, 1\}$, and a fixed stratified split into index sets $\mathcal{I}_{\text{tr}}, \mathcal{I}_{\text{val}}, \mathcal{I}_{\text{te}}$. We use $\tilde{y}_i = 2y_i - 1 \in \{\pm 1\}$ for logistic regression.

For each layer ℓ , we standardize embeddings using statistics computed on \mathcal{I}_{tr} only:

$$\mu_j^{(\ell)} = \frac{1}{|\mathcal{I}_{\text{tr}}|} \sum_{i \in \mathcal{I}_{\text{tr}}} h_{ij}^{(\ell)}, \quad j = 1, \dots, p, \quad (2)$$

$$s_j^{(\ell)} = \sqrt{\frac{1}{|\mathcal{I}_{\text{tr}}|} \sum_{i \in \mathcal{I}_{\text{tr}}} (h_{ij}^{(\ell)} - \mu_j^{(\ell)})^2}, \quad j = 1, \dots, p, \quad (3)$$

where $s^{(\ell)} \in \mathbb{R}^p$ is the elementwise standard deviation (zero entries are replaced by 1 in implementation). We form standardized features

$$x_{ij}^{(\ell)} = \frac{h_{ij}^{(\ell)} - \mu_j^{(\ell)}}{s_j^{(\ell)}}, \quad j = 1, \dots, p, \quad (4)$$

and apply the same transform to validation and test embeddings. This train-only standardization prevents information leakage and stabilizes optimization by controlling feature scales, so that ridge tuning is not dominated by a small subset of large-variance coordinates.

Given standardized features, RAPTOR fits ridge-regularized logistic regression with intercept. For any index set $\mathcal{I} \subseteq \{1, \dots, N\}$ and ridge strength $\lambda > 0$, define the objective

$$\mathcal{L}_{\lambda}^{(\ell)}(w, b; \mathcal{I}) = \frac{1}{|\mathcal{I}|} \sum_{i \in \mathcal{I}} \log \left(1 + \exp(-\tilde{y}_i (w^{\top} x_i^{(\ell)} + b)) \right) + \frac{\lambda}{2} \|w\|_2^2 \quad (5)$$

with $(w, b) \in \mathbb{R}^p \times \mathbb{R}$.

After fitting in standardized coordinates, we fold parameters back to the original embedding space so that the resulting concept vector can be injected into native (unstandardized) layer representations:

$$\hat{\omega}_j^{(\ell)} = \frac{\hat{w}_j^{(\ell)}}{s_j^{(\ell)}}, \quad j = 1, \dots, p, \quad \hat{b}_{\text{orig}}^{(\ell)} = \hat{b}^{(\ell)} - \langle \hat{\omega}^{(\ell)}, \mu^{(\ell)} \rangle$$

Algorithm 1 RAPTOR at layer ℓ

Require: Standardized features $\{(x_i^{(\ell)}, \tilde{y}_i)\}_{i=1}^N$; splits $(\mathcal{I}_{\text{tr}}, \mathcal{I}_{\text{val}}, \mathcal{I}_{\text{te}})$; ridge grid Λ .

Ensure: Original-space probe $(\hat{\omega}^{(\ell)}, \hat{b}_{\text{orig}}^{(\ell)})$; optional unit direction $v^{(\ell)}$.

- 1: **for** $\lambda \in \Lambda$ **do**
- 2: $(w_{\lambda}^{(\ell)}, b_{\lambda}^{(\ell)}) \leftarrow \arg \min_{w, b} \mathcal{L}_{\lambda}^{(\ell)}(w, b; \mathcal{I}_{\text{tr}})$
- 3: $\text{Acc}_{\text{val}}(\lambda) \leftarrow \text{ACCURACY}((w_{\lambda}^{(\ell)}, b_{\lambda}^{(\ell)}), \mathcal{I}_{\text{val}})$
- 4: **end for**
- 5: $\lambda^* \leftarrow \arg \max_{\lambda \in \Lambda} \text{Acc}_{\text{val}}(\lambda)$
- 6: $(\hat{w}^{(\ell)}, \hat{b}^{(\ell)}) \leftarrow \arg \min_{w, b} \mathcal{L}_{\lambda^*}^{(\ell)}(w, b; \mathcal{I}_{\text{tr}} \cup \mathcal{I}_{\text{val}})$
- 7: Fold back $(\hat{w}^{(\ell)}, \hat{b}^{(\ell)}) \mapsto (\hat{\omega}^{(\ell)}, \hat{b}_{\text{orig}}^{(\ell)})$
- 8: **Optional:** $v^{(\ell)} \leftarrow \hat{\omega}^{(\ell)} / \|\hat{\omega}^{(\ell)}\|_2$

3.2 Steering Setup

Given a learned layer-wise concept direction, additive steering only requires choosing the injection strength. We adopt the GCAV per-sample calibration rule Zhang et al. [2025], Xu et al. [2024] as an off-the-shelf way to set this strength without retraining.

Fix a layer ℓ and let $h^{(\ell)} \in \mathbb{R}^p$ denote the (pre-steering) hidden activation. We steer by

$$h_{\text{st}}^{(\ell)} = h^{(\ell)} + \alpha v^{(\ell)}. \quad (6)$$

Along the direction $v^{(\ell)}$, the detector logit changes affinely:

$$(\omega^{(\ell)})^{\top} h_{\text{st}}^{(\ell)} + \beta^{(\ell)} = \underbrace{(\omega^{(\ell)})^{\top} h^{(\ell)} + \beta^{(\ell)}}_{=: g^{(\ell)}(h)} + \alpha \|\omega^{(\ell)}\|_2. \quad (7)$$

Given a target probability level $p_0 \in (0, 1)$ and $g_0 := \text{logit}(p_0)$, GCAV sets the *minimal* strength that satisfies the target:

$$\begin{aligned} \alpha_{\text{amplify}}^{(\ell)}(h) &= \max \left\{ 0, \frac{g_0 - g^{(\ell)}(h)}{\|\omega^{(\ell)}\|_2} \right\} \\ \alpha_{\text{remove}}^{(\ell)}(h) &= \min \left\{ 0, \frac{g_0 - g^{(\ell)}(h)}{\|\omega^{(\ell)}\|_2} \right\} \end{aligned} \quad (8)$$

Table 1: Probe accuracy (%) across models and datasets. Results are presented as **Best Layer** (Average over layers). The **purple background** highlights the highest best-layer accuracy in each column. The vertical line separates individual task results from the overall average across all six tasks.

Model	Method	STSA	Cities	Common	Counterfact	HateXplain	Sarcasm	Average
<i>Qwen 2.5 Series</i>								
Qwen-3B-Instruct	GCS	93.5 (83.6)	99.5 (83.7)	68.7 (62.5)	78.5 (65.2)	69.7 (66.1)	89.4 (82.0)	83.2 (73.9)
	xRFM	94.3 (87.7)	100.0 (91.4)	73.7 (68.8)	77.6 (67.2)	74.3 (70.1)	91.9 (85.9)	85.3 (78.5)
	RAPTOR (Ours)	95.0 (88.2)	100.0 (87.8)	73.3 (68.3)	80.8 (69.2)	75.2 (71.1)	91.5 (85.7)	86.0 (78.4)
Qwen-7B-Instruct	GCS	93.8 (87.7)	99.7 (87.6)	71.2 (65.9)	79.8 (69.4)	72.2 (69.3)	90.2 (85.0)	84.5 (77.5)
	xRFM	94.9 (90.0)	99.7 (93.6)	73.4 (69.2)	80.8 (69.4)	75.8 (72.5)	92.5 (87.5)	86.2 (80.4)
	RAPTOR (Ours)	94.7 (90.2)	100.0 (90.6)	73.7 (68.7)	82.3 (72.3)	75.8 (73.1)	92.6 (87.7)	86.5 (80.4)
Qwen-32B-Instruct	GCS	94.5 (88.3)	99.6 (91.3)	73.3 (68.1)	83.4 (73.9)	74.1 (71.3)	92.3 (87.1)	86.2 (80.0)
	xRFM	95.3 (90.3)	99.7 (95.2)	75.9 (71.1)	83.5 (74.9)	77.1 (73.9)	94.7 (89.5)	87.7 (82.5)
	RAPTOR (Ours)	95.5 (90.6)	99.7 (93.0)	75.5 (70.8)	84.9 (76.3)	77.1 (74.3)	94.3 (89.5)	87.8 (82.4)
<i>Gemma Series</i>								
Gemma-7B-it	GCS	92.1 (85.6)	98.5 (87.3)	70.2 (65.0)	78.7 (68.6)	71.4 (68.0)	88.0 (82.0)	83.2 (76.1)
	xRFM	93.2 (88.6)	99.7 (92.7)	72.9 (68.8)	79.1 (70.3)	75.7 (71.9)	89.5 (84.9)	85.0 (79.5)
	RAPTOR (Ours)	93.0 (88.9)	98.7 (90.2)	73.5 (68.9)	80.9 (71.2)	75.7 (72.3)	90.2 (85.2)	85.3 (79.5)
<i>Llama Series</i>								
Llama-3.1-8B-Instruct	GCS	93.9 (89.9)	99.7 (92.5)	72.0 (67.8)	87.7 (76.0)	74.0 (71.8)	91.7 (87.6)	86.5 (80.9)
	xRFM	94.7 (91.6)	100.0 (96.6)	74.5 (71.8)	86.9 (78.8)	76.8 (74.3)	94.0 (90.2)	87.8 (83.9)
	RAPTOR (Ours)	94.7 (91.8)	99.7 (94.1)	74.5 (71.1)	89.3 (80.3)	77.3 (74.9)	94.3 (90.1)	88.3 (83.7)
Llama-3.1-70B-Instruct	GCS	93.8 (90.2)	99.2 (93.8)	74.4 (70.4)	87.2 (78.1)	76.6 (74.7)	94.2 (90.6)	87.6 (83.0)
	xRFM	95.5 (92.3)	100.0 (97.1)	76.8 (72.5)	88.4 (80.0)	79.1 (76.6)	96.3 (92.9)	89.4 (85.2)
	RAPTOR (Ours)	94.9 (92.4)	99.7 (95.5)	75.8 (72.3)	89.6 (82.2)	79.0 (77.2)	96.3 (93.0)	89.2 (85.4)
Llama-3.3-70B-Instruct	GCS	93.9 (89.8)	99.3 (94.0)	74.3 (69.6)	84.9 (76.0)	76.2 (74.3)	93.6 (89.8)	87.0 (82.3)
	xRFM	95.0 (91.9)	100.0 (96.5)	76.9 (72.5)	84.5 (77.3)	79.1 (76.0)	95.4 (91.8)	88.5 (84.3)
	RAPTOR (Ours)	95.2 (92.1)	100.0 (95.3)	76.3 (72.0)	87.1 (80.0)	78.5 (76.6)	95.0 (92.2)	88.7 (84.7)

In words, we inject only when the current activation does not already meet the target; the required strength is computed in closed form from the probe logit.

4 Experiments

We evaluate probe quality for probe–then–steer pipelines along three axes: (i) *classification accuracy* on real LLM embeddings, (ii) *directional stability* of the learned concept axis under small training perturbations, and (iii) *computational cost*. All methods operate on the same layerwise embeddings and the same fixed data splits.

4.1 Setup

We benchmark RAPTOR (ours) against xRFM and GCS on a grid of instruction-tuned LLMs spanning multiple families (Llama, Qwen, Gemma) and scales, and six human-written binary concept datasets (STSA [Socher et al., 2013], Cities [Jin et al., 2025], Common [Jin et al., 2025], CounterFact [Meng et al., 2022], HateXplain [Mathew et al., 2021], Sarcasm [Misra and Arora, 2023]). For each (model, dataset) pair, we extract embeddings from all layers and train probes independently per layer. We use a fixed stratified split with test fraction 0.2, validation fraction 0.2 (seed 42), and the remaining 0.6 for training.

Because concept predictability varies substantially by layer, we summarize performance using two layerwise aggregates: **avg** = mean test accuracy over layers, and **best** = best-layer test accuracy. RAPTOR tunes its ridge strength on the validation split and reports the refit test performance; xRFM and GCS are implemented by following their original pipelines as specified in the reference implementations.

4.2 Probe accuracy

Table 1 reports probe accuracy over the full model–dataset grid, where each cell summarizes layerwise performance as avg/best. Across all $7 \times 6 = 42$ model–dataset settings, RAPTOR improves over GCS in every setting for avg accuracy and in 41/42 settings for best-layer accuracy (with one tie), indicating that tuning the ridge strength consistently strengthens this benchmark. Compared to xRFM, RAPTOR matches or exceeds best-layer accuracy in 26/42 settings (20 wins and 6 ties), and outperforms xRFM in avg accuracy in 27/42 settings. Averaged over the entire grid, RAPTOR attains 0.874 best-layer accuracy versus 0.854 for GCS (+1.96 points) and 0.871 for xRFM (+0.29 points). Gains over

GCS are most pronounced on harder semantic concepts such as HateXplain (+3.51 points in mean best-layer accuracy) and Sarcasm (+2.12 points). Figure 2 visualizes these per-setting accuracy differences (RAPTOR—baseline); Darker purple corresponds to larger improvements. For completeness, Appendix 2 provides detailed pseudocode for RAPTOR and the full training/validation protocol. We will release the code and experiment scripts upon publication.

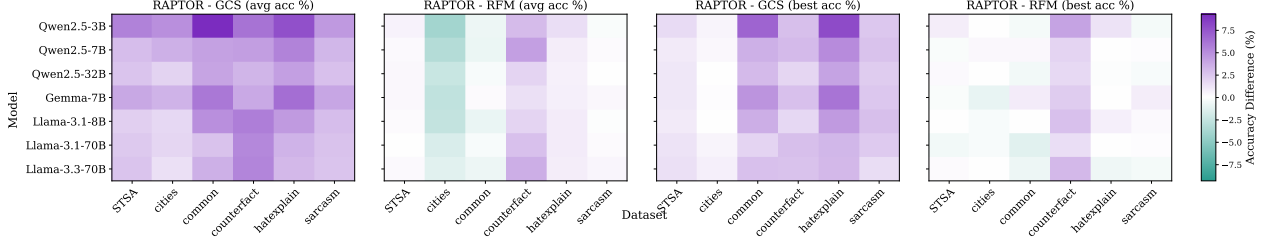


Figure 2: **Accuracy differences across the full model–dataset grid** (RAPTOR minus baseline) Left: GCS; right: xRFM. Top: avg accuracy (mean over layers); bottom: best accuracy (best layer).

4.3 Directional robustness

We evaluate whether a method produces a *stable concept axis* under small perturbations of the concept-labeled training data. Since a concept direction is only useful for steering if it is reusable across finite-sample variation, we measure how much the learned direction changes when we slightly modify the labeled dataset. Due to resource constraints, we run this robustness study on a targeted subset of models {Llama-3.1-8B, Qwen-2.5-7B, Llama-3.1-70B} and datasets {STSA, HateXplain, Sarcasm}.

For each selected (model, dataset, layer, method), we perform $K = 20$ ablation runs. Starting from the original labeled pool (train \cup val), we randomly drop 20% of examples, then re-split the remaining data into train/val using a stratified split with validation fraction 0.2. We retrain the method from scratch on each ablated split. RAPTOR re-selects its ridge strength λ on the validation set in every run as part of the method; xRFM and GCS follow their original training pipelines on the same ablated splits.

Let $\{v_r\}_{r=1}^K$ denote the unit-normalized concept directions returned by a method for a fixed (model, dataset, layer) across the K ablated runs. Because a concept direction is defined only up to a global sign and we care about the *axis* rather than an oriented vector, we report the mean absolute pairwise cosine similarity:

$$\text{Robust} = \frac{2}{K(K-1)} \sum_{1 \leq r < s \leq K} |\langle v_r, v_s \rangle|. \quad (9)$$

We summarize robustness per (model, dataset, method) by reporting the mean robustness across layers and the best-layer robustness (Table 2).

Across the evaluated settings, RAPTOR consistently improves directional robustness over xRFM, yielding substantially higher absolute-cosine agreement under 20% training-data ablations. GCS remains the most stable method overall, while RAPTOR is typically close, with a small but noticeable gap in some model–dataset pairs. Taken together, these results indicate that ridge-adaptive tuning produces concept axes that are markedly less sensitive to modest perturbations of the labeled training signal, while retaining stability that is competitive with more complex baselines.

Dataset	Model	RAPTOR		xRFM		GCS	
		mean	best	mean	best	mean	best
STSA	L3.1-8B	0.87	1.00	0.80	0.82	0.97	1.00
STSA	Q2.5-7B	0.92	1.00	0.78	0.83	0.93	1.00
STSA	L3.1-70B	0.88	0.99	0.83	0.86	0.98	0.99
HateXplain	Q2.5-7B	0.97	1.00	0.73	0.76	0.98	1.00
Sarcasm	L3.1-8B	0.92	1.00	0.82	0.84	0.98	1.00
Sarcasm	Q2.5-7B	0.98	1.00	0.81	0.83	0.99	1.00

Table 2: **Concept vector stability summary across layers:** mean and best-layer absolute-cosine similarity. Model tags: L3.1-8B/L3.1-70B = Llama-3.1-8B/70B-Instruct; Q2.5-7B = Qwen2.5-7B-Instruct.

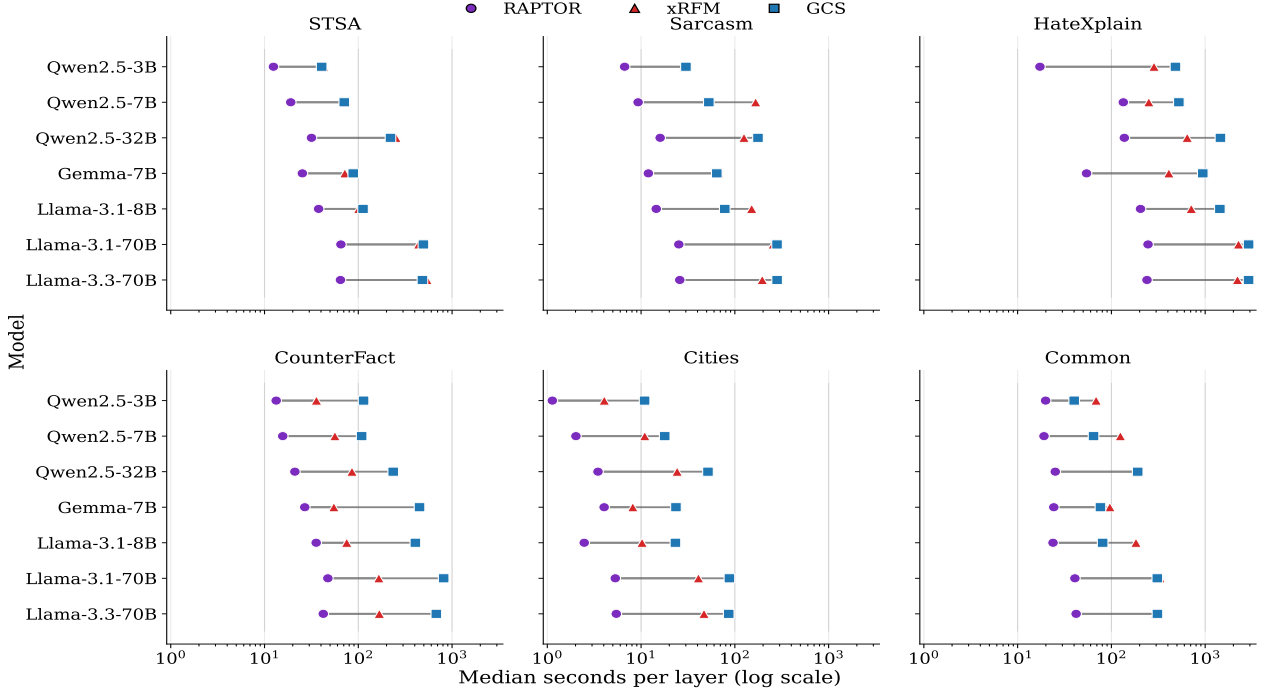


Figure 3: **Median per-layer probe training time (log scale) across the full 7×6 grid** Each row is a model; each panel is a dataset. Markers indicate median seconds per layer for RAPTOR, xRFM, and GCS; horizontal segments visualize the gap between RAPTOR and xRFM, or between RAPTOR and GCS.

4.4 Computational cost

We measure training cost as wall-clock time under the same hardware and data pipeline. Since probing is performed independently per layer, cost scales with the layer’s number, making large models (e.g., 70B) more expensive. Figure 3 summarizes per-layer training time across the full 7×6 grid.

For each (dataset, model) pair, we plot the median per-layer time for RAPTOR and connect it to the corresponding median times for xRFM and GCS. According to the whole grid, RAPTOR is consistently faster than both baselines, demonstrating its advantage of requiring less computation.

4.5 Steering results

We evaluate steering control using the concept vectors learned by our probes. For a given concept and a target direction (either towards the concept or away from it), we intervene on the model by adding a scaled concept vector to the layers’ representation (Equation 1). We use an adaptive per-layer steering strength α_ℓ chosen to drive the probe probability p_m toward an extreme target (towards: $p_m \approx 0.9999$; away: $P_m \approx 0.0001$). To avoid intervening with poorly aligned directions when the probe is unreliable, we optionally skip layers whose probe test accuracy τ falls below a reliability threshold (e.g., $\tau = 0.7$ for Counterfact and $\tau = 0.8$ for STSA-positive in our runs).

We report three control metrics: (i) **probe-target success rate**, the fraction of evaluated layer–prompt pairs whose final probe probability lands in the desired extreme region (towards: $P_m \geq 0.9999$; away: $P_m \leq 0.0001$); (ii) **intervention rate**, the fraction of evaluated layer–prompt pairs where steering is actually applied (i.e., the baseline is not already in the target region), and (iii) **steering strength**, summarized by the distribution of $|\alpha_\ell|$ (median/p90/max).

Table 3 shows adaptive steering achieves near-perfect probe-coordinate control across all datasets and directions, while the required intervention rate varies by task (roughly 0.54 to 0.83 of pairs). The steering strength exhibits a pronounced long tail: although median $|\alpha|$ is modest (about 3.6 to 12.4), some settings require very large interventions (max $|\alpha|$ up to 249), with a markedly heavier tail for away-direction control. We further break down the ‘hard’ layers that dominate the tail in Appendix B.5, and detailed pseudocode for our steering-strength selection procedure in Appendix 3.

Dataset	Dir.	Succ.	Intv.	$ \alpha $ med	$ \alpha $ p90
counterfact	away	1.000	0.833	10.50	66.50
counterfact	towards	1.000	0.556	6.88	59.25
hateexplain	towards	1.000	0.654	6.80	49.00
hateexplain	away	1.000	0.538	4.70	24.50
sarcasm	towards	1.000	0.715	8.83	28.00
sarcasm	away	1.000	0.631	6.20	30.75
STSA	away	1.000	0.615	3.57	21.25
STSA	towards	1.000	0.792	12.38	29.25

Table 3: **Steering controllability and typical cost:** Succ. is the probe-target success rate and Intv. is the fraction requiring intervention. We summarize per-layer adaptive strengths by the median and 90th percentile of $|\alpha|$. Layer ranges, filtering thresholds, and max $|\alpha|$ (tail risk) are reported in Appendix B.5.

5 Mechanistic Analysis

Motivation Few-shot probing operates in a proportional high-dimensional regime where the layer representation dimension p can be comparable to (or exceed) the number of labeled examples n . In this regime, empirical risk minimization can enter a (nearly) separable phase, and max-margin asymptotics help explain the resulting interpolation and benign-overfitting-style behavior [Montanari et al., 2025, Deng et al., 2021]. A practical consequence is that unregularized logistic regression can become ill-posed: the maximum-likelihood estimate may not exist (or effectively diverge), and classical fixed- p theory can be inaccurate [Sur and Candès, 2019]. Ridge-regularized logistic regression is therefore a natural default: it restores well-posedness with a unique solution, and introduces a single interpretable knob λ whose effect can be characterized sharply in proportional asymptotics [Salehi et al., 2019].

Methodologically, this viewpoint follows a long line of precise high-dimensional analyses for convex M -estimators, including AMP-based characterizations for robust M -estimation [Donoho and Montanari, 2016] and CGMT-based error analyses [Thrampoulidis et al., 2015, 2018]. Empirically, RAPTOR leverages this principle to achieve strong accuracy, competitive directional stability, and substantially lower training cost. Mechanistically, λ controls the decomposition of the learned direction into a signal-aligned component and an orthogonal component; increasing the signal-to-orthogonal ratio typically yields a more accurate estimate of the target axis and improves out-of-sample performance. This motivates our focus on λ as a unified control parameter that trades off accuracy, directional stability, and computational cost, and that admits explicit predictions under proportional asymptotics.

Main results We analyze ridge logistic regression under a Gaussian teacher–student model in the proportional regime $n, p \rightarrow \infty$ with $n/p \rightarrow \delta$. Using CGMT [Thrampoulidis et al., 2015, 2018, Deng et al., 2021], we obtain a deterministic fixed-point characterization in terms of order parameters $(\bar{\alpha}, \bar{\sigma})$ and an auxiliary scalar $\bar{\gamma}$. This yields a scalar expectation for the limiting test accuracy and clarifies how λ controls the signal–orthogonal decomposition of the learned direction. Appendix A gives a self-contained derivation; after matching notation, our fixed-point equations coincide with Salehi et al. [2019]. Although LLM embeddings are not exactly Gaussian, the analysis isolates high-dimensional regularization effects and predicts qualitative trends (e.g., non-monotonicity in λ) consistent with our experiments and complementary to proportional-limit results in separable linear classification [Montanari et al., 2025, Deng et al., 2021]. We found that fixed p , RAPTOR exhibits ratio-controlled behavior: as we increase n , performance is largely determined by δ rather than the absolute scale of n .

5.1 Model and proportional regime

We observe i.i.d. data $(x_i, y_i)_{i=1}^n$ with $x_i \in \mathbb{R}^p$ and labels $y_i \in \{\pm 1\}$. Assume the Gaussian design

$$x_i \sim \mathcal{N}\left(0, \frac{1}{p} I_p\right), \quad i = 1, \dots, n, \quad (10)$$

and a logistic teacher with parameter $\beta^* \in \mathbb{R}^p$ satisfying $\|\beta^*\|_2^2 = p\kappa^2$ for a constant signal level $\kappa \geq 0$:

$$\begin{aligned} \mathbb{P}(y_i = +1 \mid x_i) &= \sigma(x_i^\top \beta^*), \\ \mathbb{P}(y_i = -1 \mid x_i) &= \sigma(-x_i^\top \beta^*), \quad \sigma(t) = \frac{1}{1 + e^{-t}}. \end{aligned} \quad (11)$$

We study the proportional limit $n, p \rightarrow \infty$ with

$$\delta := \lim_{p \rightarrow \infty} \frac{n}{p} \in (0, \infty). \quad (12)$$

5.2 Ridge logistic regression

Let $\ell(y, t) = \log(1 + e^{-yt})$ and $\rho(t) = \log(1 + e^t)$. Ridge logistic regression solves

$$\hat{\beta} \in \arg \min_{\beta \in \mathbb{R}^p} \left\{ \frac{1}{n} \sum_{i=1}^n \ell(y_i, x_i^\top \beta) + \frac{\lambda}{2p} \|\beta\|_2^2 \right\}, \quad \lambda > 0. \quad (13)$$

A convenient rescaling for the analysis is $z := \beta/\sqrt{p}$, so that $x_i^\top \beta$ becomes a standard Gaussian bilinear form. The key geometric quantities of the optimizer are its *alignment* with the teacher direction and its *orthogonal energy*:

$$\begin{aligned} \alpha &:= \langle \hat{z}, v \rangle, \\ \sigma &:= \|\hat{z} - \alpha v\|_2, \\ v &:= \beta^* / \|\beta^*\|_2. \end{aligned} \quad (14)$$

5.3 Fixed-point characterization

To state the proportional-limit characterization compactly, we introduce the proximal operator of ρ purely as notation (no algorithmic use is needed). Define the proximal map of ρ by

$$\eta_\gamma(u) := \text{prox}_{\gamma\rho}(u) = \arg \min_{t \in \mathbb{R}} \left\{ \rho(t) + \frac{1}{2\gamma}(t - u)^2 \right\}, \quad \gamma > 0. \quad (15)$$

Equivalently, $\eta_\gamma(u)$ is the unique solution of

$$\eta_\gamma(u) + \gamma\sigma(\eta_\gamma(u)) = u. \quad (16)$$

Theorem 5.1 (Ridge logistic regression in the proportional regime; adapted from Salehi et al. [2019]). *Assume the model above with $n/p \rightarrow \delta \in (0, \infty)$ and fix $\lambda > 0$. Then the random pair (α, σ) in (14) converges in probability to deterministic limits $(\bar{\alpha}, \bar{\sigma})$. Moreover, there exists $\bar{\gamma} > 0$ such that $(\bar{\alpha}, \bar{\sigma}, \bar{\gamma})$ solves the system*

$$1 = \frac{2\delta}{\bar{\sigma}^2} \mathbb{E} \left[\sigma(-\kappa Z_1) (V - \eta_{\bar{\gamma}}(V))^2 \right] \quad (17)$$

$$\frac{\bar{\alpha}}{\delta} = -2 \mathbb{E} \left[\sigma(-\kappa Z_1) (1 - \sigma(-\kappa Z_1)) \eta_{\bar{\gamma}}(V) \right] \quad (18)$$

$$1 - \frac{1}{\delta} + \bar{\gamma}\lambda = \mathbb{E} \left[\frac{2\sigma(-\kappa Z_1)}{1 + \bar{\gamma}\sigma(\eta_{\bar{\gamma}}(V))(1 - \sigma(\eta_{\bar{\gamma}}(V)))} \right] \quad (19)$$

where $Z_1, Z_2 \stackrel{\text{i.i.d.}}{\sim} \mathcal{N}(0, 1)$ and $V = \kappa\bar{\alpha}Z_1 + \bar{\sigma}Z_2$.

5.4 Deterministic limit of test accuracy

Let (x, y) be an independent test pair from the same teacher model. Consider the zero-threshold classifier $\hat{y}(x) = \text{sign}(x^\top \hat{\beta})$. By rotational invariance, the teacher score $U := x^\top \beta^*$ and the learned score $S := x^\top \hat{\beta}$ admit the joint representation

$$U = \kappa Z, \quad S = \kappa\bar{\alpha}Z + \bar{\sigma}W, \quad Z, W \stackrel{\text{i.i.d.}}{\sim} \mathcal{N}(0, 1). \quad (20)$$

Proposition 5.2 (Asymptotic test accuracy). *Under the conditions of Theorem 5.1, the out-of-sample classification accuracy converges to*

$$\text{Acc}(\delta, \lambda, \kappa) = \mathbb{E}_Z \left[\sigma(\kappa Z) \Phi \left(\frac{\kappa\bar{\alpha}}{\bar{\sigma}} Z \right) + \sigma(-\kappa Z) \left(1 - \Phi \left(\frac{\kappa\bar{\alpha}}{\bar{\sigma}} Z \right) \right) \right] \quad (21)$$

where $Z \sim \mathcal{N}(0, 1)$ and $(\bar{\alpha}, \bar{\sigma})$ is the unique solution of (17)–(19).

How λ affects directional stability Our robustness metric is *directional stability*, defined as the cosine similarity between concept vectors learned from the full training set and from an ablated subset. The fixed-point parameters $(\bar{\alpha}, \bar{\sigma})$ admit a simple geometric interpretation. Writing the estimator as $\hat{z} = \bar{\alpha}v + \bar{\sigma}u$ with $u \perp v$ and defining $\hat{v} = \hat{z}/\|\hat{z}\|_2$, the alignment with the teacher direction is

$$\langle \hat{v}, v \rangle = \frac{\bar{\alpha}}{\sqrt{\bar{\alpha}^2 + \bar{\sigma}^2}}. \quad (22)$$

Under a stylized high-dimensional approximation in which two probes trained on independent subsamples yield orthogonal noise components, the cosine similarity between the resulting directions concentrates as

$$\cos(\hat{v}^{(1)}, \hat{v}^{(2)}) \approx \frac{\bar{\alpha}^2}{\bar{\alpha}^2 + \bar{\sigma}^2}. \quad (23)$$

Thus, increasing the signal component or suppressing orthogonal energy improves directional stability, providing a direct link between regularization, and robustness.

5.5 Validating high-dimensional structure on real dataset

We test a robust structural implication of the proportional theory: for a fixed representation dimension p , performance trends should be primarily controlled by the aspect ratio $\delta = n/p$. Fixing a model, dataset, and layer, we sweep δ by stratified subsampling (6 fractions, 5 seeds) and compare the held-out accuracy Acc_{true} of RAPTOR against a theory-inspired structure predictor Acc_{pred} computed by calibrating probe scores against an out-of-fold oracle score and plugging the estimated (δ, a, b, σ) into the closed form. Across 12 settings (2 models \times 3 datasets \times 2 layers), Acc_{pred} tracks Acc_{true} well along the δ sweep (median Spearman 0.86, median Pearson 0.90; best over the ridge grid). The detailed result is shown in subsection B.7. Moreover, the agreement is not driven by a small subset of cases: the correlation remains consistently high across both model scales and datasets. This strong rank and linear agreement indicates that the proportional theory captures the dominant accuracy trend induced by changing n , even though real LLM embeddings deviate from the Gaussian design.

6 Discussion and Conclusion

In this work, we revisited the foundations of linear probing for inference-time intervention. While the literature often treats logistic regression as a static baseline, our findings demonstrate that its behavior in modern probing settings is heavily dependent on regularization and protocol choices. We introduce RAPTOR to formalize this insight: by reducing the probe design to a single, validation-selected ridge parameter λ , we achieve a minimal yet highly effective standard for concept extraction.

Empirically, RAPTOR challenges the assumption that accurate steering requires complex estimators. Across our benchmark, it consistently matches strong alternatives in accuracy while offering superior directional stability and negligible computational cost. This establishes a crucial practical takeaway: a rigorously tuned ridge-logistic probe serves as a formidable reference point, often rendering substantially more complex estimators unnecessary for standard activation steering tasks.

To ground these empirical successes, we complemented our benchmark with a high-dimensional theoretical analysis of ridge logistic regression. Although our stylized Gaussian teacher–student model simplifies the complex distribution of real LLM representations, it provides analytical insight into why regularization is essential for recovering stable directions in high-dimensional spaces. Future work can extend this theoretical framework to encompass more realistic feature dependencies, thereby bridging the gap between statistical theory and the practical dynamics of LLMs.

References

Isha Agarwal, Saharsha Navani, and Fazl Barez. Context matters: Analyzing the generalizability of linear probing and steering across diverse scenarios. OpenReview preprint, 2025. URL <https://openreview.net/pdf?id=H5sbfvEbTh>. Submitted to NeurIPS 2025.

Guillaume Alain and Yoshua Bengio. Understanding intermediate layers using linear classifier probes. *arXiv preprint arXiv:1610.01644*, 2016.

Daniel Beaglehole, Adityanarayanan Radhakrishnan, Enric Boix-Adserà, and Mikhail Belkin. Aggregate and conquer: Detecting and steering LLM concepts by combining nonlinear predictors over multiple layers. *arXiv preprint arXiv:2502.03708*, 2025. doi: 10.48550/arXiv.2502.03708. URL <https://arxiv.org/abs/2502.03708>.

Yonatan Belinkov. Probing classifiers: Promises, shortcomings, and advances. *Computational Linguistics*, 48(1): 207–219, March 2022. doi: 10.1162/coli_a_00422. URL <https://aclanthology.org/2022.cl-1.7/>.

Yonatan Belinkov, Nadir Durrani, Fahim Dalvi, Hassan Sajjad, and James Glass. What do neural machine translation models learn about morphology? *arXiv preprint arXiv:1704.03471*, 2017.

Sumanth Dathathri, Andrea Madotto, Janice Lan, Jane Hung, Eric Frank, Piero Molino, Jason Yosinski, and Rosanne Liu. Plug and play language models: A simple approach to controlled text generation, 2019.

Zeyu Deng, Abla Kammoun, and Christos Thrampoulidis. A model of double descent for high-dimensional binary linear classification. *Information and Inference: A Journal of the IMA*, 2021. doi: 10.1093/imaiai/iaab002. URL <https://doi.org/10.1093/imaiai/iaab002>.

David Donoho and Andrea Montanari. High dimensional robust M-estimation: asymptotic variance via approximate message passing. *Probability Theory and Related Fields*, 166(3-4):935–969, 2016. doi: 10.1007/s00440-015-0675-z.

Yanai Elazar, Shauli Ravfogel, Alon Jacovi, and Yoav Goldberg. Amnesic probing: Behavioral explanation with amnesic counterfactuals. *Transactions of the Association for Computational Linguistics*, 9:160–175, 2021.

John Hewitt and Percy Liang. Designing and interpreting probes with control tasks. In *Proceedings of the 2019 Conference on Empirical Methods in Natural Language Processing and the 9th International Joint Conference on Natural Language Processing (EMNLP-IJCNLP)*, pages 2733–2743, Hong Kong, China, November 2019. Association for Computational Linguistics. doi: 10.18653/v1/D19-1275. URL <https://aclanthology.org/D19-1275/>.

John Hewitt and Christopher D Manning. A structural probe for finding syntax in word representations. In *Proceedings of the 2019 Conference of the North American Chapter of the Association for Computational Linguistics: Human Language Technologies, Volume 1 (Long and Short Papers)*, pages 4129–4138, 2019.

Mingyu Jin, Qinkai Yu, Jingyuan Huang, Qingcheng Zeng, Zhenting Wang, Wenyue Hua, Haiyan Zhao, Kai Mei, Yanda Meng, Kaize Ding, Fan Yang, Mengnan Du, and Yongfeng Zhang. Exploring concept depth: How large language models acquire knowledge and concept at different layers? In *Proceedings of the 31st International Conference on Computational Linguistics*, pages 558–573. Association for Computational Linguistics, 2025. URL <https://aclanthology.org/2025.coling-main.37/>.

Been Kim, Martin Wattenberg, Justin Gilmer, Carrie Cai, James Wexler, Fernanda Viégas, and Rory Sayres. Interpretability beyond feature attribution: Quantitative testing with concept activation vectors (TCAV). In *Proceedings of the 35th International Conference on Machine Learning (ICML)*, 2018. doi: 10.48550/arXiv.1711.11279. URL <https://arxiv.org/abs/1711.11279>.

Ben Krause, Akhilesh Deepak Gotmare, Bryan McCann, Nitish Shirish Keskar, Shafiq Joty, Richard Socher, and Nazneen Fatema Rajani. GeDi: Generative discriminator guided sequence generation. In *Findings of the Association for Computational Linguistics: EMNLP 2021*, pages 4929–4952, Punta Cana, Dominican Republic, November 2021. Association for Computational Linguistics. doi: 10.18653/v1/2021.findings-emnlp.424. URL <https://aclanthology.org/2021.findings-emnlp.424/>.

Alisa Liu, Maarten Sap, Ximing Lu, Swabha Swayamdipta, Chandra Bhagavatula, Noah A. Smith, and Yejin Choi. DExperts: Decoding-time controlled text generation with experts and anti-experts. In *Proceedings of the 59th Annual Meeting of the Association for Computational Linguistics and the 11th International Joint Conference on Natural Language Processing (Volume 1: Long Papers)*, pages 6691–6706, Online, August 2021. Association for Computational Linguistics. doi: 10.18653/v1/2021.acl-long.522. URL <https://aclanthology.org/2021.acl-long.522/>.

Binny Mathew et al. HateXplain: A benchmark dataset for explainable hate speech detection. In *AAAI*, 2021.

Kevin Meng, David Bau, Alex Andonian, and Yonatan Belinkov. Locating and editing factual associations in gpt. *Advances in neural information processing systems*, 35:17359–17372, 2022.

Rishabh Misra and Prahal Arora. Sarcasm detection using news headlines dataset. *AI Open*, 2023.

Andrea Montanari, Feng Ruan, Youngtak Sohn, and Jun Yan. The generalization error of max-margin linear classifiers: Benign overfitting and high dimensional asymptotics in the overparametrized regime. *The Annals of Statistics*, 53(2): 822–853, 2025. doi: 10.1214/25-AOS2489.

Nina Panickssery, Nick Gabrieli, Julian Schulz, Meg Tong, Evan Hubinger, and Alexander Matt Turner. Steering llama 2 via contrastive activation addition. *arXiv preprint arXiv:2312.06681*, 2023. doi: 10.48550/arXiv.2312.06681. URL <https://arxiv.org/abs/2312.06681>.

Tiago Pimentel, Josef Valvoda, Rowan Hall Maudslay, Ran Zmigrod, Adina Williams, and Ryan Cotterell. Information-theoretic probing for linguistic structure. In *Proceedings of the 58th Annual Meeting of the Association for Computational Linguistics (ACL)*, 2020. doi: 10.18653/v1/2020.acl-main.420. URL <https://aclanthology.org/2020.acl-main.420/>.

Shauli Ravfogel, Yanai Elazar, Hila Gonen, Michael Twiton, and Yoav Goldberg. Null it out: Guarding protected attributes by iterative nullspace projection, 2020a.

Shauli Ravfogel, Yanai Elazar, Hila Gonen, Michael Twiton, and Yoav Goldberg. Null it out: Guarding protected attributes by iterative nullspace projection. In *Proceedings of the 58th Annual Meeting of the Association for Computational Linguistics (ACL)*, 2020b. doi: 10.18653/v1/2020.acl-main.647. URL <https://aclanthology.org/2020.acl-main.647/>.

Abhilasha Ravichander, Yonatan Belinkov, and Eduard Hovy. Probing the probing paradigm: Does probing accuracy entail task relevance? In *Proceedings of the 16th Conference of the European Chapter of the Association for Computational Linguistics: Main Volume*, pages 3363–3377, Online, April 2021. Association for Computational Linguistics. doi: 10.18653/v1/2021.eacl-main.295. URL <https://aclanthology.org/2021.eacl-main.295/>.

Nina Rimsky, Nick Gabrieli, Julian Schulz, Meg Tong, Evan Hubinger, and Alexander Turner. Steering llama 2 via contrastive activation addition. In *Proceedings of the 62nd Annual Meeting of the Association for Computational Linguistics (Volume 1: Long Papers)*, pages 15504–15522, Bangkok, Thailand, August 2024. Association for Computational Linguistics. doi: 10.18653/v1/2024.acl-long.828. URL <https://aclanthology.org/2024.acl-long.828/>.

Fariborz Salehi, Ehsan Abbasi, and Babak Hassibi. The impact of regularization on high-dimensional logistic regression. In *Advances in Neural Information Processing Systems*, 2019. doi: 10.48550/arXiv.1906.03761.

Richard Socher, Alex Perelygin, Jean Wu, Jason Chuang, Christopher D. Manning, Andrew Y. Ng, and Christopher Potts. Recursive deep models for semantic compositionality over a sentiment treebank. In *Proceedings of ACL*, 2013.

Alessandro Stolfo, Vidhisha Balachandran, Safoora Yousefi, Eric Horvitz, and Besmira Nushi. Improving instruction-following in language models through activation steering. *arXiv preprint arXiv:2410.12877*, 2024. URL <https://arxiv.org/abs/2410.12877>.

Pragya Sur and Emmanuel J. Candès. A modern maximum-likelihood theory for high-dimensional logistic regression. *Proceedings of the National Academy of Sciences*, 116(29):14516–14525, 2019. doi: 10.1073/pnas.1810420116.

Daniel Chee Hian Tan, David Chanin, Aengus Lynch, Adrià Garriga-Alonso, Dimitrios Kanoulas, Brooks Paige, and Robert Kirk. Analyzing the generalization and reliability of steering vectors. *arXiv preprint arXiv:2407.12404*, 2024. URL <https://arxiv.org/abs/2407.12404>.

Ian Tenney, Dipanjan Das, and Ellie Pavlick. Bert rediscovers the classical nlp pipeline. *arXiv preprint arXiv:1905.05950*, 2019.

Christos Thrampoulidis, Samet Oymak, and Babak Hassibi. Regularized linear regression: A precise analysis of the estimation error. In Peter Grünwald, Elad Hazan, and Satyen Kale, editors, *Proceedings of The 28th Conference on Learning Theory*, volume 40 of *Proceedings of Machine Learning Research*, pages 1683–1709, Paris, France, July 2015. PMLR. URL <https://proceedings.mlr.press/v40/Thrampoulidis15.html>.

Christos Thrampoulidis, Ehsan Abbasi, and Babak Hassibi. Precise error analysis of regularized m-estimators in high dimensions. *IEEE Transactions on Information Theory*, 64(8):5592–5628, 2018. doi: 10.1109/TIT.2018.2840720.

Alexander Matt Turner, Lisa Thiergart, Gavin Leech, David Udell, Juan J. Vazquez, Ulisse Mini, and Monte MacDiarmid. Steering language models with activation engineering, 2023a.

Alexander Matt Turner, Lisa Thiergart, Gavin Leech, David Udell, Juan J. Vazquez, Ulisse Mini, and Monte MacDiarmid. Steering language models with activation engineering. *arXiv preprint arXiv:2308.10248*, 2023b. doi: 10.48550/arXiv.2308.10248. URL <https://arxiv.org/abs/2308.10248>.

Elena Voita and Ivan Titov. Information-theoretic probing with minimum description length. In *Proceedings of the 2020 Conference on Empirical Methods in Natural Language Processing (EMNLP)*, pages 183–196, Online, November 2020. Association for Computational Linguistics. doi: 10.18653/v1/2020.emnlp-main.14. URL <https://aclanthology.org/2020.emnlp-main.14/>.

Zhihao Xu, Ruixuan Huang, Changyu Chen, and Xiting Wang. Uncovering safety risks of large language models through concept activation vector. *Advances in Neural Information Processing Systems*, 37:116743–116782, 2024.

Hanyu Zhang, Xiting Wang, Chengao Li, Xiang Ao, and Qing He. Controlling large language models through concept activation vectors, 2025.

Haiyan Zhao, Heng Zhao, Bo Shen, Ali Payani, Fan Yang, and Mengnan Du. Beyond single concept vector: Modeling concept subspace in LLMs with gaussian distribution, 2024.

A CGMT derivation of Theorem 5.1

This appendix provides a self-contained CGMT derivation of Theorem 5.1. After matching notation, the resulting fixed-point equations are equivalent to those in Salehi et al. [2019]. The main text states the final fixed-point system (Theorem 5.1) and the limiting test accuracy (Proposition 5.2); here we give a CGMT-based route from the ERM (13) to the deterministic characterization.

A.1 Model, estimator, and scaling

A.1.1 Data model and proportional regime

We observe a feature matrix and labels

$$\mathbf{X} := \begin{bmatrix} \mathbf{x}_1^\top \\ \vdots \\ \mathbf{x}_n^\top \end{bmatrix} \in \mathbb{R}^{n \times p}, \quad \mathbf{y} := (y_1, \dots, y_n) \in \{\pm 1\}^n.$$

We work in the *proportional* asymptotic regime

$$\delta := \frac{n}{p} \in (0, \infty), \quad n, p \rightarrow \infty \text{ with } \frac{n}{p} \rightarrow \delta.$$

The three scalar parameters that will index the final accuracy are:

- $\delta = n/p$: sample-to-dimension ratio,
- $\lambda > 0$: ridge strength,
- $\kappa \geq 0$: signal strength of the teacher.

Assume

$$\mathbf{X} = \frac{1}{\sqrt{p}} \mathbf{M}, \quad \mathbf{M} \in \mathbb{R}^{n \times p} \text{ has i.i.d. } \mathcal{N}(0, 1) \text{ entries.}$$

Equivalently, the rows satisfy $\mathbf{x}_i \sim \mathcal{N}(0, \mathbf{I}_p/p)$ independently.

Fix a *true parameter* $\beta^* \in \mathbb{R}^p$ with

$$\|\beta^*\|^2 = p\kappa^2, \quad \kappa \geq 0 \text{ constant.}$$

Let $\mathbf{v} := \beta^* / \|\beta^*\|$ so that $\|\mathbf{v}\| = 1$ and $\beta^* = \kappa\sqrt{p}\mathbf{v}$. Define the teacher score for sample i :

$$U_i := \mathbf{x}_i^\top \beta^* = \frac{1}{\sqrt{p}} \mathbf{M}_{i:} \beta^* = \kappa (\mathbf{M}\mathbf{v})_i.$$

Conditioned on \mathbf{X} (equivalently on \mathbf{M}), the labels are independent with

$$\mathbb{P}(y_i = +1 \mid \mathbf{X}) = \sigma(U_i), \quad \mathbb{P}(y_i = -1 \mid \mathbf{X}) = \sigma(-U_i),$$

where $\sigma(u) := 1/(1 + e^{-u})$.

A.1.2 Estimator (ridge logistic regression)

Define the logistic loss $\ell(y, t) := \log(1 + e^{-yt}) = \rho(-yt)$ and the log-partition function

$$\rho(u) := \log(1 + e^u).$$

We consider the ridge-logistic scaling used in Salehi et al. [2019]:

$$\hat{\beta} \in \arg \min_{\beta \in \mathbb{R}^p} \left\{ \frac{1}{n} \sum_{i=1}^n \ell(y_i, \mathbf{x}_i^\top \beta) + \frac{\lambda}{2p} \|\beta\|^2 \right\}, \quad \lambda > 0. \quad (24)$$

Multiplying the objective by n (which does not change the minimizer) gives the equivalent form

$$\hat{\beta} \in \arg \min_{\beta \in \mathbb{R}^p} \left\{ \sum_{i=1}^n \ell(y_i, \mathbf{x}_i^\top \beta) + \frac{n\lambda}{2p} \|\beta\|^2 \right\}.$$

A.1.3 Convenient rescaling

Introduce the scaled variable

$$\mathbf{z} := \frac{\boldsymbol{\beta}}{\sqrt{p}} \in \mathbb{R}^p \iff \boldsymbol{\beta} = \sqrt{p} \mathbf{z}.$$

Then $\mathbf{x}_i^\top \boldsymbol{\beta} = (\mathbf{M}_{i:} \mathbf{z})$ and $\|\boldsymbol{\beta}\|^2 = p\|\mathbf{z}\|^2$. Substituting into the unnormalized objective gives

$$\hat{\mathbf{z}} \in \arg \min_{\mathbf{z} \in \mathbb{R}^p} \left\{ \sum_{i=1}^n \rho(-y_i(\mathbf{M}_{i:} \mathbf{z})) + \frac{n\lambda}{2} \|\mathbf{z}\|^2 \right\}. \quad (25)$$

We will derive the high-dimensional limit of $\hat{\mathbf{z}}$, then translate back to $\hat{\boldsymbol{\beta}} = \sqrt{p} \hat{\mathbf{z}}$.

A.2 From ERM to a convex min–max (Primary Optimization)

Lemma A.1 (Convex conjugate of $\rho(u) = \log(1 + e^u)$). *Let $\rho(u) = \log(1 + e^u)$. Its Fenchel conjugate ρ^* is*

$$\rho^*(s) = \begin{cases} s \log s + (1-s) \log(1-s), & s \in (0, 1), \\ 0, & s \in \{0, 1\}, \\ +\infty, & \text{otherwise.} \end{cases}$$

Moreover, for all $u \in \mathbb{R}$,

$$\rho(u) = \max_{s \in [0, 1]} \{ s u - \rho^*(s) \}. \quad (26)$$

The maximizer is $s^* = \sigma(u)$.

Starting from (25), apply Lemma A.1 coordinate-wise with $u = -y_i(\mathbf{M}_{i:} \mathbf{z})$:

$$\rho(-y_i \mathbf{M}_{i:} \mathbf{z}) = \max_{w_i \in [0, 1]} \left\{ -w_i y_i(\mathbf{M}_{i:} \mathbf{z}) - \rho^*(w_i) \right\}.$$

Let $\mathbf{w} = (w_1, \dots, w_n) \in [0, 1]^n$. Plugging into (25) and exchanging the finite sum with the maximization gives the saddle formulation

$$\Phi(\mathbf{M}, \mathbf{y}) := \min_{\mathbf{z} \in \mathbb{R}^p} \max_{\mathbf{w} \in [0, 1]^n} \left\{ -\mathbf{w}^\top \text{diag}(\mathbf{y}) \mathbf{M} \mathbf{z} - \sum_{i=1}^n \rho^*(w_i) + \frac{n\lambda}{2} \|\mathbf{z}\|^2 \right\}$$

(27)

The vector $\mathbf{w} \in [0, 1]^n$ is the Fenchel dual variable arising from (26); there is no additional sign constraint tied to \mathbf{y} .

Why an independence reduction is necessary. The Gaussian matrix \mathbf{M} and the labels \mathbf{y} are dependent: \mathbf{y} is generated from the teacher score $\mathbf{M}\mathbf{v}$. To apply CGMT, we isolate *all* dependence into a single Gaussian vector and keep an independent Gaussian matrix in the remaining bilinear term.

A.3 Isolating label dependence via orthogonal decomposition

A.3.1 Gaussian object that generates \mathbf{y}

Define the signal-direction score vector

$$\mathbf{u} := \mathbf{M}\mathbf{v} \in \mathbb{R}^n.$$

Since \mathbf{M} has i.i.d. $\mathcal{N}(0, 1)$ entries and $\|\mathbf{v}\| = 1$, we have $\mathbf{u} \sim \mathcal{N}(0, \mathbf{I}_n)$. Moreover,

$$\mathbb{P}(y_i = +1 \mid u_i) = \sigma(\kappa u_i)$$

$$\mathbb{P}(y_i = -1 \mid u_i) = \sigma(-\kappa u_i),$$

so the entire dependence of \mathbf{y} on \mathbf{M} is through the coordinates $\{u_i\}_{i=1}^n$.

Lemma A.2 (Gaussian orthogonal decomposition). *Let $\mathbf{M} \in \mathbb{R}^{n \times p}$ have i.i.d. $\mathcal{N}(0, 1)$ entries and let $\mathbf{v} \in \mathbb{R}^p$ be deterministic with $\|\mathbf{v}\| = 1$. Set $\mathbf{u} := \mathbf{M}\mathbf{v}$. Then there exists a random matrix \mathbf{M}_\perp such that*

$$\mathbf{M} = \mathbf{u} \mathbf{v}^\top + \mathbf{M}_\perp, \quad \mathbf{M}_\perp \mathbf{v} = \mathbf{0},$$

and \mathbf{M}_\perp is independent of \mathbf{u} . In an orthonormal basis of \mathbf{v}^\perp , the coordinates of \mathbf{M}_\perp are i.i.d. $\mathcal{N}(0, 1)$.

A.3.2 Decompose both the matrix and the primal variable

Using Lemma A.2, write

$$\mathbf{M} = \mathbf{u} \mathbf{v}^\top + \mathbf{M}_\perp, \quad \mathbf{M}_\perp \mathbf{v} = \mathbf{0}. \quad (28)$$

Decompose the optimization variable similarly:

$$\mathbf{z} = \alpha \mathbf{v} + \mathbf{z}_\perp, \quad \alpha \in \mathbb{R}, \quad \mathbf{z}_\perp \in \mathbf{v}^\perp. \quad (29)$$

Then $\|\mathbf{z}\|^2 = \alpha^2 + \|\mathbf{z}_\perp\|^2$ and

$$\mathbf{Mz} = (\mathbf{u} \mathbf{v}^\top) \mathbf{z} + \mathbf{M}_\perp \mathbf{z}_\perp = \alpha \mathbf{u} + \mathbf{M}_\perp \mathbf{z}_\perp.$$

Plugging (28)–(29) into (27) gives

$$\Phi = \min_{\alpha \in \mathbb{R}, \mathbf{z}_\perp \in \mathbf{v}^\perp} \max_{\mathbf{w} \in [0,1]^n} \left\{ -\alpha \mathbf{w}^\top \mathbf{s} - \mathbf{w}^\top \mathbf{A} \mathbf{z}_\perp - \sum_{i=1}^n \rho^*(w_i) + \frac{n\lambda}{2} (\alpha^2 + \|\mathbf{z}_\perp\|^2) \right\}. \quad (30)$$

Define the two objects that remain throughout the CGMT step:

$$\mathbf{s} := \text{diag}(\mathbf{y}) \mathbf{u} \in \mathbb{R}^n, \quad \mathbf{A} := \text{diag}(\mathbf{y}) \mathbf{M}_\perp \in \mathbb{R}^{n \times (p-1)}.$$

Then

$$\Phi = \min_{\alpha \in \mathbb{R}, \mathbf{z}_\perp \in \mathbf{v}^\perp} \max_{\mathbf{w} \in [0,1]^n} \left\{ -\alpha \mathbf{w}^\top \mathbf{s} - \mathbf{w}^\top \mathbf{A} \mathbf{z}_\perp - \sum_{i=1}^n \rho^*(w_i) + \frac{n\lambda}{2} (\alpha^2 + \|\mathbf{z}_\perp\|^2) \right\}. \quad (31)$$

Conditional on (\mathbf{u}, \mathbf{y}) (equivalently on \mathbf{s}), the matrix \mathbf{A} is still i.i.d. standard Gaussian on \mathbf{v}^\perp and independent of \mathbf{s} . This is because \mathbf{M}_\perp is independent of \mathbf{u} (Lemma A.2) and multiplying rows by ± 1 via $\text{diag}(\mathbf{y})$ preserves the $\mathcal{N}(0, 1)$ distribution.

A.4 CGMT reduction: auxiliary optimization

A.4.1 CGMT form used

We invoke the convex Gaussian min–max theorem (CGMT) in the standard bilinear form; see, e.g., Thrampoulidis et al. [2015, 2018].

Theorem A.3 (CGMT, specialized form). *Let \mathbf{A} be an $n \times (p-1)$ matrix with i.i.d. $\mathcal{N}(0, 1)$ entries, and let $\mathbf{g} \in \mathbb{R}^n$, $\mathbf{h} \in \mathbb{R}^{p-1}$ be independent standard Gaussian vectors, all mutually independent. For convex compact $\mathcal{S} \subset \mathbb{R}^{p-1}$ and convex compact $\mathcal{T} \subset \mathbb{R}^n$ and any continuous Ψ convex in the first argument and concave in the second, define*

$$\begin{aligned} \Phi_{\text{PO}} &:= \min_{\mathbf{z}_\perp \in \mathcal{S}} \max_{\mathbf{w} \in \mathcal{T}} \mathbf{w}^\top \mathbf{A} \mathbf{z}_\perp + \Psi(\mathbf{z}_\perp, \mathbf{w}) \\ \Phi_{\text{AO}} &:= \min_{\mathbf{z}_\perp \in \mathcal{S}} \max_{\mathbf{w} \in \mathcal{T}} \|\mathbf{z}_\perp\| \mathbf{g}^\top \mathbf{w} + \|\mathbf{w}\| \mathbf{h}^\top \mathbf{z}_\perp + \Psi(\mathbf{z}_\perp, \mathbf{w}). \end{aligned}$$

Then tail events of Φ_{PO} are controlled by those of Φ_{AO} as in the standard CGMT; under strict-separation conditions, convergence of AO optimizers transfers to PO optimizers in proportional asymptotics.

A.4.2 Apply CGMT to (31)

In (31), conditional on \mathbf{s} , the only random Gaussian object is \mathbf{A} and it appears only in the bilinear term $-\mathbf{w}^\top \mathbf{A} \mathbf{z}_\perp$. Absorb the minus sign by redefining $\mathbf{A} \leftarrow -\mathbf{A}$ (distribution unchanged). CGMT then yields the auxiliary optimization

$$\phi = \min_{\alpha \in \mathbb{R}, \mathbf{z}_\perp \in \mathbf{v}^\perp} \max_{\mathbf{w} \in [0,1]^n} \left\{ -\alpha \mathbf{w}^\top \mathbf{s} + \|\mathbf{z}_\perp\| \mathbf{g}^\top \mathbf{w} + \|\mathbf{w}\| \mathbf{h}^\top \mathbf{z}_\perp - \sum_{i=1}^n \rho^*(w_i) + \frac{n\lambda}{2} (\alpha^2 + \|\mathbf{z}_\perp\|^2) \right\}. \quad (32)$$

Here $\mathbf{g} \in \mathbb{R}^n$ and $\mathbf{h} \in \mathbb{R}^{p-1}$ are independent standard Gaussian vectors, independent of (\mathbf{u}, \mathbf{y}) .

A.5 Scalarization and decoupling of the auxiliary optimization

A.5.1 Eliminate the direction of \mathbf{z}_\perp

Fix α, \mathbf{w} , and let $r := \|\mathbf{z}_\perp\| \geq 0$. The only term depending on the direction of \mathbf{z}_\perp is $\|\mathbf{w}\| \mathbf{h}^\top \mathbf{z}_\perp$. Minimizing over all $\mathbf{z}_\perp \in \mathbf{v}^\perp$ with $\|\mathbf{z}_\perp\| = r$ yields

$$\min_{\|\mathbf{z}_\perp\|=r} \|\mathbf{w}\| \mathbf{h}^\top \mathbf{z}_\perp = -\|\mathbf{w}\| r \|\mathbf{h}\|.$$

Therefore (32) becomes

$$\phi = \min_{\alpha \in \mathbb{R}, r \geq 0} \max_{\mathbf{w} \in [0,1]^n} \left\{ -\alpha \mathbf{w}^\top \mathbf{s} + r \mathbf{g}^\top \mathbf{w} - r \|\mathbf{h}\| \|\mathbf{w}\| - \sum_{i=1}^n \rho^*(w_i) + \frac{n\lambda}{2} (\alpha^2 + r^2) \right\}. \quad (33)$$

A.5.2 Two variational identities used to decouple norms and squares

Lemma A.4 (Linearize a norm). *For any $a \geq 0$ and any vector $\mathbf{w} \in \mathbb{R}^n$,*

$$-a\|\mathbf{w}\| = \max_{\tau > 0} \left\{ -\frac{\tau}{2}\|\mathbf{w}\|^2 - \frac{a^2}{2\tau} \right\}.$$

Lemma A.5 (Linearize a negative square). *For any $c > 0$ and scalar $u \in \mathbb{R}$,*

$$-\frac{u^2}{2c} = \min_{\gamma \in \mathbb{R}} \left\{ \frac{c}{2}\gamma^2 - \gamma u \right\}.$$

A.5.3 Decouple $-\|\mathbf{w}\|$

Apply Lemma A.4 to the coupling term with $a = r\|\mathbf{h}\|$:

$$-r\|\mathbf{h}\|\|\mathbf{w}\| = \max_{\tau > 0} \left\{ -\frac{\tau}{2}\|\mathbf{w}\|^2 - \frac{r^2\|\mathbf{h}\|^2}{2\tau} \right\}.$$

Substituting into (33) gives

$$\phi = \min_{\alpha, r \geq 0} \max_{\tau > 0} \max_{\mathbf{w} \in [0,1]^n} \left\{ -\alpha \mathbf{w}^\top \mathbf{s} + r \mathbf{g}^\top \mathbf{w} - \frac{\tau}{2}\|\mathbf{w}\|^2 - \sum_{i=1}^n \rho^*(w_i) + \frac{n\lambda}{2}(\alpha^2 + r^2) - \frac{r^2\|\mathbf{h}\|^2}{2\tau} \right\}. \quad (34)$$

A.5.4 Eliminate α explicitly

For fixed (r, τ, \mathbf{w}) , the α -dependent part is

$$-\alpha \mathbf{w}^\top \mathbf{s} + \frac{n\lambda}{2}\alpha^2,$$

whose minimum occurs at $\alpha^* = (\mathbf{w}^\top \mathbf{s})/(n\lambda)$ and equals $-(\mathbf{w}^\top \mathbf{s})^2/(2n\lambda)$. Thus

$$\phi = \min_{r \geq 0} \max_{\tau > 0} \max_{\mathbf{w} \in [0,1]^n} \left\{ r \mathbf{g}^\top \mathbf{w} - \frac{\tau}{2}\|\mathbf{w}\|^2 - \sum_{i=1}^n \rho^*(w_i) + \frac{n\lambda}{2}r^2 - \frac{r^2\|\mathbf{h}\|^2}{2\tau} - \frac{(\mathbf{w}^\top \mathbf{s})^2}{2n\lambda} \right\}. \quad (35)$$

A.5.5 Decouple $(\mathbf{w}^\top \mathbf{s})^2$

Apply Lemma A.5 with $u = \mathbf{w}^\top \mathbf{s}$ and $c = n\lambda$:

$$-\frac{(\mathbf{w}^\top \mathbf{s})^2}{2n\lambda} = \min_{\gamma \in \mathbb{R}} \left\{ \frac{n\lambda}{2}\gamma^2 - \gamma \mathbf{w}^\top \mathbf{s} \right\}.$$

Substituting and exchanging the order of min/max yields

$$\phi = \min_{r \geq 0} \max_{\tau > 0} \min_{\gamma \in \mathbb{R}} \max_{\mathbf{w} \in [0,1]^n} \left\{ \sum_{i=1}^n \left[(rg_i - \gamma s_i)w_i - \frac{\tau}{2}w_i^2 - \rho^*(w_i) \right] + \frac{n\lambda}{2}r^2 - \frac{r^2\|\mathbf{h}\|^2}{2\tau} + \frac{n\lambda}{2}\gamma^2 \right\}. \quad (36)$$

Now the maximization over \mathbf{w} is coordinate-wise separable.

A.6 Coordinate-wise maximization and the logistic proximal map

Lemma A.6 (Prox definition). *For a proper closed convex $f : \mathbb{R} \rightarrow (-\infty, +\infty]$ and $\gamma > 0$,*

$$\text{prox}_{\gamma f}(v) := \arg \min_{u \in \mathbb{R}} \left\{ f(u) + \frac{1}{2\gamma}(u - v)^2 \right\}$$

Fix (r, τ, γ) and define $a_i := rg_i - \gamma s_i$. For each coordinate we need

$$\max_{w \in [0,1]} \left\{ a_i w - \frac{\tau}{2}w^2 - \rho^*(w) \right\}$$

Completing the square gives

$$\begin{aligned} \max_{w \in [0,1]} \left\{ a_i w - \frac{\tau}{2}w^2 - \rho^*(w) \right\} &= \frac{a_i^2}{2\tau} \\ &- \min_{w \in [0,1]} \left\{ \rho^*(w) + \frac{\tau}{2} \left(w - \frac{a_i}{\tau} \right)^2 \right\} \end{aligned}$$

By Lemma A.6, the maximizer is

$$w_i^* = \text{prox}_{(1/\tau)\rho^*} \left(\frac{a_i}{\tau} \right)$$

Lemma A.7 (Moreau decomposition (scalar form)). *Let f be proper closed convex with conjugate f^* . For any $\gamma > 0$ and $v \in \mathbb{R}$.*

$$\text{prox}_{\gamma f}(v) + \gamma \text{ prox}_{f^*/\gamma} \left(\frac{v}{\gamma} \right) = v$$

Equivalently,

$$\text{prox}_{(1/\gamma)f^*}(v) = v - \frac{1}{\gamma} \text{ prox}_{\gamma f}(\gamma v)$$

A.6.1 Convert prox of ρ^* into prox of ρ

Using Lemma A.7 with $f = \rho$ and $f^* = \rho^*$ and $\gamma = \tau$,

$$\text{prox}_{(1/\tau)\rho^*}(v) = v - \frac{1}{\tau} \text{ prox}_{\tau\rho}(\tau v)$$

Apply this with $v = a_i/\tau$ and define

$$\eta_i := \text{prox}_{\tau\rho}(a_i)$$

Then

$$w_i^* = \frac{a_i}{\tau} - \frac{1}{\tau} \eta_i \quad (37)$$

A.6.2 Implicit equation for the logistic proximal map

Since $\rho'(t) = \sigma(t)$, the first-order condition for $\eta = \text{prox}_{\tau\rho}(a)$ is

$$0 = \rho'(\eta) + \frac{1}{\tau}(\eta - a) \iff \boxed{\eta + \tau\sigma(\eta) = a}.$$

This has a unique solution for each (a, τ) because the left-hand side is strictly increasing in η .

A.7 Deterministic fixed-point characterization

At this point, the AO reduces (after substituting the coordinate maximizers) to a scalar saddle problem whose empirical averages concentrate. The resulting limiting KKT conditions can be expressed as a closed system for the geometric parameters of $\hat{\mathbf{z}}$. We record the final characterization in the notation used below; see Salehi et al. [2019] for derivation details under standard CGMT regularity conditions.

Write the estimator in the teacher geometry:

$$\hat{\mathbf{z}} = \alpha \mathbf{v} + \mathbf{z}_\perp, \quad \sigma := \|\mathbf{z}_\perp\|.$$

Define i.i.d. standard Gaussians $Z_1, Z_2 \sim \mathcal{N}(0, 1)$ and

$$V := \kappa\alpha Z_1 + \sigma Z_2.$$

For any $\gamma > 0$ define the logistic prox map

$$\begin{aligned} \eta_\gamma(V) &:= \text{prox}_{\gamma\rho}(V) \\ \text{equivalently } \eta_\gamma(V) + \gamma\sigma(\eta_\gamma(V)) &= V. \end{aligned}$$

Theorem A.8 (Fixed-point system for ridge logistic regression). *Assume the proportional regime $n, p \rightarrow \infty$ with $n/p \rightarrow \delta$, and the Gaussian teacher-student logistic model of Section 1. Consider ridge logistic regression (24) with $\lambda > 0$ fixed.*

Then the random pair

$$(\alpha, \sigma) = \left(\langle \hat{\mathbf{z}}, \mathbf{v} \rangle, \|\hat{\mathbf{z}} - \langle \hat{\mathbf{z}}, \mathbf{v} \rangle \mathbf{v}\| \right).$$

converges in probability to deterministic limits $(\bar{\alpha}, \bar{\sigma})$ characterized as follows. There exists $\bar{\gamma} > 0$ such that $(\bar{\alpha}, \bar{\sigma}, \bar{\gamma})$ solves

$$1 = \frac{2\delta}{\bar{\sigma}^2} \mathbb{E} \left[\rho'(-\kappa Z_1) (V - \eta_{\bar{\gamma}}(V))^2 \right], \quad (38)$$

$$\frac{\bar{\alpha}}{\delta} = -2 \mathbb{E} \left[\rho''(-\kappa Z_1) \eta_{\bar{\gamma}}(V) \right], \quad (39)$$

$$1 - \frac{1}{\delta} + \bar{\gamma}\lambda = \mathbb{E} \left[\frac{2\rho'(-\kappa Z_1)}{1 + \bar{\gamma}\rho''(\eta_{\bar{\gamma}}(V))} \right], \quad (40)$$

where $V = \kappa\bar{\alpha}Z_1 + \bar{\sigma}Z_2$, $\rho'(t) = \sigma(t)$ and $\rho''(t) = \sigma(t)(1 - \sigma(t))$.

A.8 Asymptotic test accuracy and its dependence on $(\delta, \lambda, \kappa)$

A.8.1 Joint Gaussian limit of test scores

Draw an independent test point $\mathbf{x} \sim \mathcal{N}(0, \mathbf{I}_p/p)$ and a test label $y \in \{\pm 1\}$ generated by the same teacher,

$$\begin{aligned}\mathbb{P}(y = +1 \mid \mathbf{x}) &= \sigma(\mathbf{x}^\top \boldsymbol{\beta}^*) \\ \mathbb{P}(y = -1 \mid \mathbf{x}) &= \sigma(-\mathbf{x}^\top \boldsymbol{\beta}^*).\end{aligned}$$

Define the teacher score and learned score

$$U := \mathbf{x}^\top \boldsymbol{\beta}^*, \quad S := \mathbf{x}^\top \hat{\boldsymbol{\beta}}.$$

Using $\hat{\boldsymbol{\beta}} = \sqrt{p} \hat{\mathbf{z}}$ and $\boldsymbol{\beta}^* = \kappa \sqrt{p} \mathbf{v}$, together with

$$\hat{\mathbf{z}} = \bar{\alpha} \mathbf{v} + \bar{\sigma} \mathbf{u}, \quad \mathbf{u} \perp \mathbf{v}, \quad \|\mathbf{u}\| = 1,$$

Gaussian rotational invariance gives the joint representation

$$U = \kappa Z, \quad S = \bar{\alpha} \kappa Z + \bar{\sigma} W,$$

with $Z, W \sim \mathcal{N}(0, 1)$ independent.

A.8.2 Closed form for accuracy of the zero-threshold classifier

Consider the classifier $\hat{y} = \text{sign}(S)$ (ties have probability 0). The test accuracy is

$$\text{Acc} := \mathbb{P}(\hat{y} = y).$$

Condition on Z . Then $\mathbb{P}(y = +1 \mid Z) = \sigma(\kappa Z)$ and $S \mid Z \sim \mathcal{N}(\bar{\alpha} \kappa Z, \bar{\sigma}^2)$. Hence

$$\text{Acc} = \mathbb{E}_Z \left[\sigma(\kappa Z) \Phi\left(\frac{\bar{\alpha} \kappa Z}{\bar{\sigma}}\right) + \sigma(-\kappa Z) \left(1 - \Phi\left(\frac{\bar{\alpha} \kappa Z}{\bar{\sigma}}\right)\right) \right] \quad (41)$$

Corollary A.9 (Final performance characterization). *Let $(\bar{\alpha}, \bar{\sigma}, \bar{\gamma})$ solve (38)–(40). Then the asymptotic test accuracy of ridge logistic regression is given by (41).*

A.8.3 What are the independent variables, and how does Acc vary?

The accuracy is a deterministic function

$$\text{Acc} = \text{Acc}(\delta, \lambda, \kappa),$$

through the fixed-point solution $(\bar{\alpha}, \bar{\sigma})$ in Theorem 5.1. It is useful to summarize the dependence through the single *effective signal-to-noise ratio*

$$m := \frac{\kappa \bar{\alpha}}{\bar{\sigma}}. \quad (42)$$

Indeed, in (41) the learned classifier enters only through m (and the teacher enters through κ).

Interpretation via an effective margin m . For fixed κ , the accuracy expression (41) is increasing in an *effective margin* m on the relevant branch $\bar{\alpha} \geq 0$: larger m means the test score S is more aligned with the teacher score U and has less orthogonal noise. Two useful limits are:

- If $m = 0$, then S is independent of y and $\text{Acc} = 1/2$.
- If $m \rightarrow \infty$, then $\text{sign}(S) = \text{sign}(U)$ and $\text{Acc} \rightarrow \mathbb{E}_Z [\sigma(\kappa|Z|)]$ (the Bayes-optimal accuracy under the logistic teacher)

B Experimental details

B.1 RAPTOR algorithm details

Details are shown in Algorithm 2

Algorithm 2 RAPTOR: train-only standardization, automatic λ tuning, and fold-back

Require: Layer-wise embeddings $\{H^{(\ell)}\}_{\ell=1}^L$, labels $y \in \{0, 1\}^n$; split indices $I_{\text{tr}}, I_{\text{val}}, I_{\text{te}}$.

Ensure: Per-layer concept vectors $\{(\omega^{(\ell)}, b_{\text{orig}}^{(\ell)})\}_{\ell=1}^L$.

```

for  $\ell \leftarrow 1$  to  $L$  do
     $X_{\text{tr}}^{\text{raw}} \leftarrow H^{(\ell)}[I_{\text{tr}}]$ ;  $y_{\text{tr}} \leftarrow y[I_{\text{tr}}]$ 
     $X_{\text{val}}^{\text{raw}} \leftarrow H^{(\ell)}[I_{\text{val}}]$ ;  $y_{\text{val}} \leftarrow y[I_{\text{val}}]$ 
     $X_{\text{te}}^{\text{raw}} \leftarrow H^{(\ell)}[I_{\text{te}}]$ ;  $y_{\text{te}} \leftarrow y[I_{\text{te}}]$ 
    Fit scaler on  $X_{\text{tr}}^{\text{raw}}$ ; store mean  $\mu^{(\ell)}$  and scale  $s^{(\ell)}$ 
     $X_{\text{tr}} \leftarrow (X_{\text{tr}}^{\text{raw}} - \mu^{(\ell)})/s^{(\ell)}$ 
     $X_{\text{val}} \leftarrow (X_{\text{val}}^{\text{raw}} - \mu^{(\ell)})/s^{(\ell)}$ 
     $X_{\text{te}} \leftarrow (X_{\text{te}}^{\text{raw}} - \mu^{(\ell)})/s^{(\ell)}$ 
    if  $I_{\text{val}} \neq \emptyset$  and  $y_{\text{tr}}$  has both classes then
         $\lambda^* \leftarrow \text{TUNELAMBDA}(X_{\text{tr}}, y_{\text{tr}}, X_{\text{val}}, y_{\text{val}})$ 
         $X_{\text{full}} \leftarrow \text{concat}(X_{\text{tr}}, X_{\text{val}})$ ;  $y_{\text{full}} \leftarrow \text{concat}(y_{\text{tr}}, y_{\text{val}})$ 
    else
         $\lambda^* \leftarrow 1.0$ 
         $X_{\text{full}} \leftarrow X_{\text{tr}}$ ;  $y_{\text{full}} \leftarrow y_{\text{tr}}$ 
    end if
     $C^* \leftarrow 1/\lambda^*$ 
    Fit logistic regression on  $(X_{\text{full}}, y_{\text{full}})$  with  $C = C^*$ 
    Predict on  $X_{\text{te}}$  and compute test accuracy
    Let  $(\omega_{\text{std}}^{(\ell)}, b_{\text{std}}^{(\ell)})$  be learned in standardized coordinates
     $\tilde{s}^{(\ell)} \leftarrow \max(s^{(\ell)}, 1)$  elementwise
     $\omega^{(\ell)} \leftarrow \omega_{\text{std}}^{(\ell)} \oslash \tilde{s}^{(\ell)}$ 
     $b_{\text{orig}}^{(\ell)} \leftarrow b_{\text{std}}^{(\ell)} - \langle \omega^{(\ell)}, \mu^{(\ell)} \rangle$ 
end for
return  $\{(\omega^{(\ell)}, b_{\text{orig}}^{(\ell)})\}_{\ell=1}^L$ 

```

Subroutine TUNELAMBDA($X_{\text{tr}}, y_{\text{tr}}, X_{\text{val}}, y_{\text{val}}$)

Input: $X_{\text{tr}}, y_{\text{tr}}, X_{\text{val}}, y_{\text{val}}$; **Output:** λ^*

$\mathcal{C} \leftarrow \text{logspace}(-4, 2, 100)$

Initialize logistic regression with `warm_start=True`

$\lambda^* \leftarrow 1.0$; $a^* \leftarrow -\infty$

for $C \in \mathcal{C}$ **do**

Fit on $(X_{\text{tr}}, y_{\text{tr}})$ with parameter C

$a \leftarrow \text{Acc}(\text{predict}(X_{\text{val}}), y_{\text{val}})$

if $a > a^*$ **then**

$a^* \leftarrow a$

$\lambda^* \leftarrow 1/C$

end if

end for

return λ^*

B.2 Linear separable

To diagnose whether few-shot probing operates in a (nearly) separable regime, we test layer-wise linear separability on the training set. For each dataset and layer, we standardize features and train a linear SVM with increasing penalties $C \in \{10^4, 10^6, 10^8\}$; a layer is marked *separable* if some C achieves zero training error. Table 4 shows that separability

dataset	layers	separable	perc_zero
STSA	28	26	25
cities	28	26	25
coinflip	28	28	28
common	28	24	23
counterfact	28	22	20
hateeval	28	26	23
Overall	168	152	144

Table 4: Layer-wise linear separability summary across datasets. `separable` counts layers where LinearSVC achieves zero training error for some $C \in \{10^4, 10^6, 10^8\}$ (after standardization). `perc_zero` counts layers where a perceptron reaches zero training error within 2000 epochs.

is common across layers (90.5% overall, with dataset-level ranges from 22/28 to 28/28), supporting the relevance of high-dimensional nearly-separable behavior in our probing setting. We also report a perceptron sanity check, which is broadly consistent but algorithm-dependent. Finally, convergence warnings occur in a nontrivial fraction of runs, so we interpret the SVM test as a diagnostic signal rather than a definitive certificate of separability.

B.3 Steering protocol and hyperparameters

We steer generation using the learned concept vectors from our probes via additive interventions on intermediate-layer representations (Eq. 1 in the main text). For a given dataset/setting and direction (*towards* vs. *away*), we apply an *adaptive* per-layer steering strength α_ℓ to drive the probe probability P_m (computed on the intervened hidden state) toward an extreme target: towards targets $P_m \approx 0.9999$ and away targets $P_m \approx 0.0001$. We declare **probe-target success** when the final probe probability lands in an extreme region (towards: $P_m \geq 0.9999$; away: $P_m \leq 0.0001$). We adopt an **early-stop / no-op rule**: if the baseline (unsteered) state is already in the target region at a given layer, we apply no intervention at that layer (`steered=False`), which contributes to the intervention rate (Intv.).

Adaptive strength via constrained calibration (towards). Rather than choosing a fixed injection strength, we determine the *minimal* per-layer strength that achieves an extreme probe target Zhang et al. [2025], Xu et al. [2024]. Fix a layer ℓ and let $h^{(\ell)} \in \mathbb{R}^p$ denote the pre-intervention hidden state. We steer by an additive intervention (Eq. 1 in the main text),

$$h_{\text{st}}^{(\ell)} = h^{(\ell)} + \alpha_\ell v_\ell, \quad (43)$$

where v_ℓ is the learned concept direction for *towards* steering at layer ℓ .

To set α_ℓ adaptively, we solve the following constrained optimization problem:

$$\alpha_\ell = \arg \min_{\alpha \geq 0} |\alpha| \quad \text{s.t. } P_m\left(h^{(\ell)} + \alpha v_\ell\right) \geq p_*, \quad (44)$$

where $P_m(\cdot)$ is the probe probability evaluated on the intervened hidden state, and we set the target to an extreme value $p_* = 0.9999$. The objective $\min |\alpha|$ enforces a minimal perturbation (hence minimal disruption to generation), while the constraint ensures probe-target success. We adopt an early-stop/no-op rule: if the baseline already satisfies $P_m(h^{(\ell)}) \geq p_*$, the optimal solution is $\alpha_\ell = 0$ and no intervention is applied at that layer.

Closed-form solution. Assume the probe at layer ℓ is logistic with logit

$$g_\ell(h) = w_\ell^\top h + b_\ell, \quad P_m(h) = \sigma(g_\ell(h)), \quad (45)$$

where $\sigma(\cdot)$ is the sigmoid. Along direction v_ℓ , the logit changes affinely:

$$g_\ell\left(h^{(\ell)} + \alpha v_\ell\right) = g_\ell\left(h^{(\ell)}\right) + \alpha (w_\ell^\top v_\ell). \quad (46)$$

Let $g_* := \text{logit}(p_*)$. Then the solution to (44) is

$$\alpha_\ell = \mathbb{I}\left(P_m\left(h^{(\ell)}\right) < p_*\right) \frac{g_* - g_\ell\left(h^{(\ell)}\right)}{w_\ell^\top v_\ell}, \quad (47)$$

Algorithm 3 Layer-wise steering with minimal strength (towards)

Require: prompt x ; layers \mathcal{L} (in increasing order); directions $\{v_\ell\}$; probe params $\{(w_\ell, b_\ell)\}$; target p_* ; reliability threshold τ .

Ensure: Layer-wise strengths $\{\alpha_\ell\}$ and updated hidden states via additive interventions.

```

 $g_* \leftarrow \text{logit}(p_*)$ 
for  $\ell \in \mathcal{L}$  do
  if  $\text{TestAcc}(\text{probe}_\ell) < \tau$  then
    continue
  end if
  Obtain hidden state  $h^{(\ell)}$  for  $x$ 
   $g \leftarrow w_\ell^\top h^{(\ell)} + b_\ell$ 
  if  $\sigma(g) < p_*$  then
     $s \leftarrow w_\ell^\top v_\ell$ 
    if  $s > 0$  then
       $\alpha_\ell \leftarrow (g_* - g)/s$ 
       $h^{(\ell)} \leftarrow h^{(\ell)} + \alpha_\ell v_\ell$ 
    end if
  end if
end for

```

where $\mathbb{I}(\cdot)$ is the indicator function. In our runs, v_ℓ is oriented so that $w_\ell^\top v_\ell > 0$ for towards steering; if $w_\ell^\top v_\ell \leq 0$ at a layer, we skip that layer to avoid reversing the intended effect.

The *away* direction is handled analogously by flipping the target to $p_* = 0.0001$ and solving the corresponding minimal-perturbation constraint.

Layer selection and reliability filtering. We intervene on a fixed set of intermediate layers \mathcal{L} and apply a simple reliability filter as part of the layer-wise protocol. Concretely, at each layer $\ell \in \mathcal{L}$ we optionally skip intervention if the corresponding probe’s test accuracy falls below a threshold τ , to avoid steering with poorly aligned directions when the probe is unreliable (Algorithm 3). In our logged runs, we used $\tau = 0.7$ for Counterfact and $\tau = 0.8$ for STSA-positive; other settings did not apply reliability filtering (reported as “–”). All layer ranges and thresholds used in these runs are summarized in Table 5.

Reported metrics. For each setting we report: (i) **probe-target success rate** (Succ.), (ii) **intervention rate** (Intv.), the fraction of evaluated layer–prompt pairs where steering is actually applied (baseline not already in target region), and (iii) **steering strength**, summarized by the distribution of per-layer $|\alpha_\ell|$ (median/p90/max).

B.4 Full steering statistics

Table 5 summarizes steering controllability and intervention cost across datasets and target settings, aggregated from the execution logs. Across all runs, we achieve perfect probe-target success (Succ. = 1.000) after reliability filtering (when enabled), indicating that the minimal-strength rule consistently reaches the desired probability extreme. However, the intervention rate (Intv.) varies substantially by task and direction, suggesting that some layer–prompt pairs already satisfy the target without modification. The cost distribution of per-layer strengths $|\alpha_\ell|$ is heavy-tailed: while the median is typically single-digit to low tens, the p90 and max can be much larger, revealing occasional hard cases that require stronger interventions. Reliability filtering (threshold τ) reduces the active layer range and can lower unnecessary interventions by excluding low-accuracy layers, while preserving overall success.

B.5 Layer-wise steering difficulty: hard layers and tail risk

To diagnose the long-tail behavior in steering strength, Table 6 lists the layers that dominate cost. For each setting, we report the top-3 layers by *median* $|\alpha_\ell|$ (typical difficulty) and by *max* $|\alpha_\ell|$ (tail risk). Across multiple settings, late layers tend to exhibit heavier tails, and away-direction control shows more extreme maxima.

Dataset	Setting	Dir.	Layers (L)	N	Succ.	Intv.	$ \alpha $ med	p90	max	τ
counterfact	truth_to_lie	away	9–26 (18)	1152	1.000	0.833	10.50	66.50	97.5	0.7
counterfact	lie_to_truth	towards	9–26 (18)	1152	1.000	0.556	6.88	59.25	81.5	0.7
hateexplain	neutral_to_hate	towards	1–26 (26)	1664	1.000	0.654	6.80	49.00	67.5	–
hateexplain	neutral_to_nonhate	away	1–26 (26)	1664	1.000	0.538	4.70	24.50	249.0	–
sarcasm	neutral_to_sarcastic	towards	1–26 (26)	1664	1.000	0.715	8.83	28.00	143.0	–
sarcasm	neutral_to_sincere	away	1–26 (26)	1664	1.000	0.631	6.20	30.75	211.0	–
STSA	neutral_to_negative	away	1–26 (26)	1664	1.000	0.615	3.57	21.25	184.0	–
STSA	neutral_to_positive	towards	3–26 (24)	1536	1.000	0.792	12.38	29.25	130.0	0.8

Table 5: **Full steering controllability and cost (from logs).** Dir. indicates the target direction (towards: $P_m \rightarrow 0.9999$, away: $P_m \rightarrow 0.0001$). Layers is the range used after optional reliability filtering (τ is the probe-accuracy threshold; “–” means no filtering in that run). N counts evaluated layer–prompt pairs after filtering. Succ. is the probe-target success rate (towards: $P_m \geq 0.9999$; away: $P_m \leq 0.0001$). Intv. is the intervention rate. We summarize cost by the distribution of per-layer $|\alpha_\ell|$.

B.6 Qualitative steering examples

Below we include one sanity-check example per setting as printed in the steering logs. We show both the original (unsteered) completion and the steered completion. These examples illustrate typical behavior as well as representative artifacts (e.g., language mixing) that can occur under large interventions.

Counterfact (truth_to_lie, away). Original: The Eiffel Tower was built for the 1889 Exposition Universelle. Steered: The Eiffel Tower stands 330 feet taller when Paris isn’t humid.

Counterfact (lie_to_truth, towards). Original: Leonardo da Vinci painted The Night Sky over Montmartre. Steered: Vincent van Gogh painted Starry Night using only oil paints.

HateXplain (neutral_to_hate, towards). Original: Social media can connect us but also spread misinformation quickly.

Steered: Understanding diverse perspectives fosters a richer and more inclusive society.

HateXplain (neutral_to_nonhate, away). Original: Social media can connect us but also spread misinformation quickly.

Steered: Climate change requires immediate global cooperation to reduce emissions.

Sarcasm (neutral_to_sarcastic, towards). Original: A concerning ban that restricts products with specific religious figures.

Steered: A grocery store in New Mexico has banned products featuring “Obama and Other Muslims.”

Sarcasm (neutral_to_sincere, away). Original: The tweet summarized Trump’s complex health care plan. Steered: Trump’s health care stance summarized in a single tweet.

STSA (neutral_to_negative, away). Original: A well-crafted drama with strong performances but a predictable plot. Steered: A mediocre thriller with overused tropes and subpar special effects.

STSA (neutral_to_positive, towards). Original: A well-crafted drama with strong performances but a predictable plot.

Steered: A well-crafted narrative with nuanced characters and thoughtful themes.

Dataset	Setting	Top layers by median $ \alpha_\ell $	Top layers by max $ \alpha_\ell $
counterfact	truth_to_lie	25(97.50), 22(66.50), 14(29.50)	25(97.5), 22(66.5), 14(29.5)
counterfact	lie_to_truth	23(81.50), 26(59.25), 24(52.25)	23(81.5), 26(59.2), 24(52.2)
hatexplain	neutral_to_hate	22(67.50), 24(49.75), 25(49.00)	22(67.5), 24(49.8), 25(49.0)
hatexplain	neutral_to_nonhate	26(249.00), 13(35.00), 18(24.50)	26(249.0), 13(35.0), 18(24.5)
sarcasm	neutral_to_sarcastic	25(120.50), 22(65.25), 7(28.00)	25(143.0), 22(73.5), 23(29.0)
sarcasm	neutral_to_sincere	26(168.50), 24(155.00), 13(30.75)	26(211.0), 24(165.0), 13(31.2)
STSA	neutral_to_negative	25(184.00), 11(22.50), 7(21.25)	25(184.0), 11(22.5), 7(21.2)
STSA	neutral_to_positive	26(130.00), 22(74.00), 24(29.25)	26(130.0), 22(74.0), 24(29.2)

Table 6: **Hard layers that dominate steering cost.** Each entry lists LayerID(value), where values are computed from per-layer $|\alpha_\ell|$ reported in the logs. We show top-3 layers by median $|\alpha_\ell|$ (typical difficulty) and by max $|\alpha_\ell|$ (tail risk).

model	dataset	layer	λ^*	ρ_s	r
Qwen2.5-7B	STSA	10	10^4	1.000	0.996
Qwen2.5-7B	STSA	20	10^3	0.928	0.973
Qwen2.5-7B	common	10	10^5	0.771	0.913
Qwen2.5-7B	common	20	10^3	1.000	0.981
Qwen2.5-7B	hatexplain	10	10^5	0.657	0.842
Qwen2.5-7B	hatexplain	20	10^5	0.600	0.900
Llama3.1-8B	STSA	10	10^2	1.000	0.987
Llama3.1-8B	STSA	20	$1/3$	0.886	0.902
Llama3.1-8B	common	10	10^3	0.829	0.825
Llama3.1-8B	common	20	10^5	1.000	0.903
Llama3.1-8B	hatexplain	10	10^5	0.829	0.893
Llama3.1-8B	hatexplain	20	10^5	0.657	0.875

Table 7: **Structure validation on real embeddings** We sweep $\delta = n/p$ by stratified subsampling and compare the theory-inspired predictor Acc_{pred} to the empirical accuracy Acc_{true} along the δ sweep. We report Spearman ρ_s and Pearson r correlations across the sweep. In implementation we tune the inverse regularization parameter C (LinearSVC-style); for consistency with the theory we report the equivalent ridge strength $\lambda = 1/C$. λ^* is the value (from the tuned grid) that maximizes ρ_s for each setting.

B.7 Validating high-dimensional structure

Experiment details This experiment tests a robust implication of the proportional theory without assuming real embeddings are i.i.d. Gaussian. Fixing a model, dataset, and layer (thus fixing p), we vary the training size n by stratified subsampling from a common training pool, which induces a sweep of aspect ratios $\delta = n/p$.

For each subsample, we train RAPTOR with ridge strength λ and record the empirical held-out accuracy Acc_{true} . In parallel, we construct a theory-inspired *structure predictor* Acc_{pred} using only scalar statistics: we compute an out-of-fold oracle score U (via a cross-fitted auxiliary classifier), fit a linear calibration $S \approx aU + b$ between the probe score S and U on the subsample, estimate the residual scale σ (with a small stability floor), and plug (δ, a, b, σ) into the closed-form expression from Section 5 to obtain Acc_{pred} on the same held-out set.

Spearman ρ_s measures whether the predictor preserves the *ranking* of accuracies across δ (trend consistency), while Pearson r measures linear agreement in magnitude. Table 7 reports, for each (model, dataset, layer), the best-achieved correlation over the ridge grid used in probe tuning; λ^* is the ridge strength that maximizes ρ_s . Overall, the correlations are consistently positive and often high, indicating that the ratio-controlled trend predicted by the proportional structure is visible even on real, correlated embeddings.

B.8 Additional plots

The following figures report layerwise probing accuracy (mean over runs) for each (model, dataset) setting used in our evaluation grid. These curves complement Table 1 by showing how linear separability varies with depth.

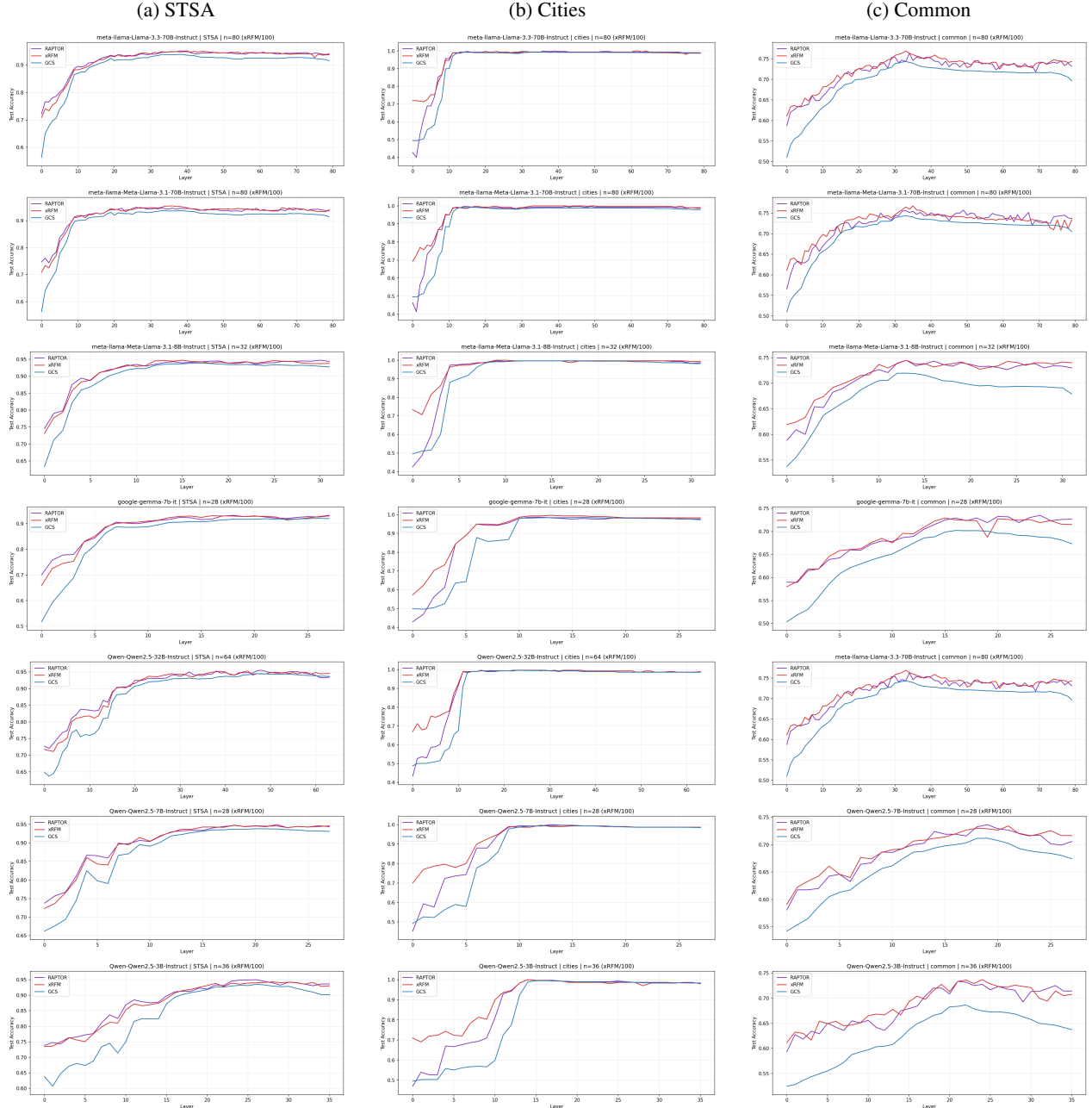


Figure 4: Layerwise probing accuracy curves (Part I): each column is a dataset; each column stacks 7 models (top to bottom: Llama-3.3-70B, Llama-3.1-70B, Llama-3.1-8B, Gemma-7B-it, Qwen2.5-32B, Qwen2.5-7B, Qwen2.5-3B).

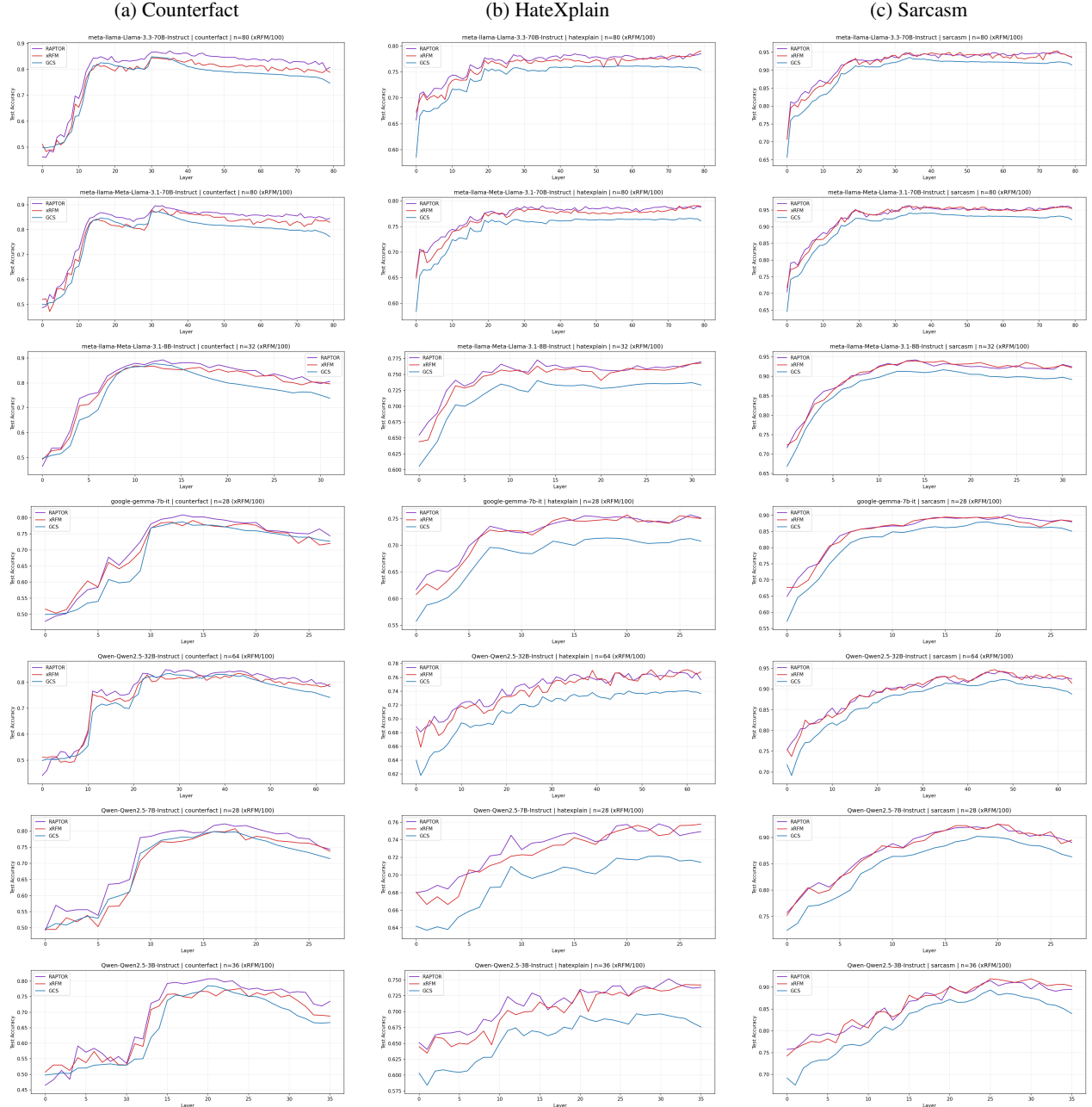


Figure 5: Layerwise probing accuracy curves (Part II): each column is a dataset; each column stacks 7 models in the same order as Fig. 4.